TOWARDS HIGH-THROUGHPUT HIGH-FREQUENCY CMOS NUCLEAR MAGNETIC RESONANCE SPECTROSCOPY

MAHTA MANSOURI

A THESIS SUBMITTED TO
THE FACULTY OF GRADUATE STUDIES
IN PARTIAL FULFILLMENT OF THE REQUIREMENTS
FOR THE DEGREE OF
MASTER OF APPLIED SCIENCE

GRADUATE PROGRAM IN
ELECTRICAL ENGINEERING AND COMPUTER SCIENCE
YORK UNIVERSITY
TORONTO, ONTARIO

May 2021

Abstract

Driven by the many of Nuclear Magnetic Resonance (NMR) spectroscopy applications, there is an ever-increasing demand for high-throughput NMR receivers to accelerate the speed and reduce the cost of the NMR spectroscopy. The envisaged solution by the industry is to employ significantly stronger static magnetic fields to achieve higher signal-to-noise ratio (SNR). However, this demands for the system to operate at proportionally-higher frequencies to satisfy the Larmor equation and to be able to shrink the receiver µcoil size (hence, fit higher number of parallel receivers in the same space) without the loss of SNR. Despite the benefits, a higher frequency of operation introduces several challenges in the design of the receiver's transducer (i.e., µcoil) and the readout circuitry (i.e., tuning, matching, and amplification circuits).

We present the design and optimization of an electromagnetic Radio Frequency (RF) µcoil along with the readout circuitry both integrated on the same silicon-based platform for fabrication in a standard 0.35-µm complementary metal-oxide-semiconductor (CMOS) technology. In the design of the µcoil, all the important electrical and physical parameters that could affect the NMR spectroscopy's overall performance are analytically identified and taken into account. Additionally, the readout integrated circuit is designed to be compatible with a wide range of on-chip and off-chip µcoils. The circuit architecture and the design procedure proposed for the readout circuit are adaptable to any frequency of operation.

The presented integrated system consists of two channels enabling simultaneous NMR spectroscopy, and has no practical limitations for channel scaling. To the best of our

knowledge, this design is the first CMOS-based NMR receiver operating at 500 MHz. While all components are designed and optimized for this frequency, the presented design procedures for both the μcoil and the readout circuits are applicable to higher frequencies.

To my parents,

For their endless love, supports and encouragements

ACKNOWLEDGMENTS

I would like to thank my supervisors, Professor Ebrahim Ghafar-zadeh and Professor Hossein Kassiri, without whom I would not have been able to complete this research, and without whom I would not have made it through my master's degree. I am grateful for their patience, consistent support and guidance throughout this project.

I would also like to thank my defense and supervisory committee, Professor Sodagar and Professor Tabatabaei, for reading my thesis and providing valuable feedback.

I would also like to acknowledge our collaborator, Dr. A. Simpson, University of Toronto, for providing informative insight regarding the NMR system and for providing an opportunity to see NMR device in action.

I am fortunate to have amazing friends that make my master's years memorable and support me during this time. My most special thanks go to my parents and brother for their unconditional love and supports during these years.

Table of Contents

List of Tables

List of Figures

Chapter 1

Introduction

1.1. An Introduction to Nuclear Magnetic Resonance Spectroscopy

Molecular structural elucidation is an initial step in the analysis of material properties [1]. The structure of the molecule is closely related to its properties, therefore exploring the structure of novel or pre-existing molecules is important in scientific and manufacturing processes [2]. Spectroscopic measurements, x-ray crystallography, and electron microscopy have been widely used to obtain molecular information [3][4][5], with the latter two being inferior to spectroscopy when it comes to measuring three-dimensional structure of molecules as well as providing unique insights on dynamics and intermolecular interactions [6].

Among spectroscopic aids researchers have at their disposal, nuclear magnetic resonance (NMR) and microwave spectroscopy are the two major tools [7], with the former being the most versatile of all spectroscopic techniques and is used for the study of a wide

range of materials including liquids, solids, and solutions [7]. NMR spectroscopy is a powerful technique to conduct bimolecular analysis that determines molecular composition and structure of samples. It has been widely deployed in a variety of applications across different fields including chemistry [8], physics [9], biology [10], material science [11], and biochemistry [12]. The detection of NMR signal was first reported in 1945 by two groups, one at Stanford University, and the other one at Harvard University. Soon after, due to the ability of performing non-destructive chemical analysis to determine molecular structure faster and simpler than previous analysis methods, NMR analysis was started to be used in almost every chemistry laboratory [13]. Another advantage of this method, is the capability of measuring spin-to-spin coupling, a measure of atomic interaction within the molecule. MRI, an imaging modality widely used in the clinics as a standard of care is an example of an application of NMR (MRI is a multidimensional NMR imaging) [13]. Other applications of NMR spectroscopy/manometry/imaging include monitoring chemical reactions in solutions as it provides detailed kinetics and mechanistic information [14], observing mixing different samples in-situ [15], as well as detecting component of a chemical sample in vivo [15], and determining the purity of a sample, and monitoring biological samples [16].

This chapter starts with explaining the principles of NMR spectroscopy and the way it operates, followed by a conclusive literature review on the state-of-the-art NMR spectroscopy devices. The chapter ends with defining the system-level design specifications and discuss the main objectives and implementation challenges of this work.

1.2. NMR Principles

NMR is a physical phenomenon based on the absorption and re-emitting of weak Radio Frequency (RF) electromagnetic signals produced by the sample's nuclei in the presence of a strong static magnetic field. NMR spectroscopy aims to monitor the local magnetic field around the nuclei that is responsible for changing the resonance frequency. Due to the uniqueness of this field for each chemical compound, this technique allows us to learn about details of the molecule structure, or to identify complex molecules inside a sample. [17].

A simplified illustration of an NMR spectroscopy system is shown in Figure 1-1. As shown, a typical NMR system consists of: (1) a giant primary magnet creating a uniform strong constant magnetic field (B_0), (2) an excitation coil, connected to a pulse generator, creating a weak oscillating magnetic field (B_1), and (3) a sample holder comprised of (3.1) a receiving/detection coil connected to a spectrometer, working as the transducer, (3.2) a substrate for holding the sample in the proximity of the receiving coil, (4) a tuning and shimming circuitry Built with a number of capacitors, inductors, and resistors, (5) a spectrometer, and (6) a computer for displaying/processing the recorded data.

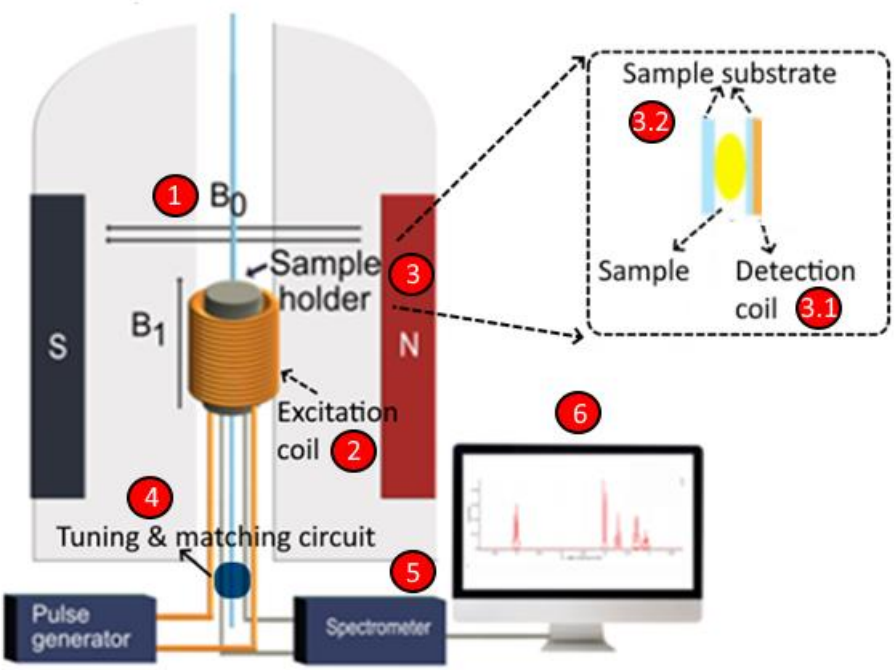

Figure 1-1 A simplified illustration of the NMR spectroscopy system (electrical components are not shown here for simplicity).

An NMR spectroscopy system works in two modes: excitation and relaxation. During the excitation mode an external current is applied to the excitation coil creating a weak oscillating magnetic field (B_1). Excitation mode leads to changes in the sample's magnetization and nuclear spin orientation. then the external current is turned off, hence eliminating B1, effectively starting the relaxation mode. In this mode, the re-emitted signals generated due to the sample's nuclear spin reorientation, contains valuable information about the sample structure that should be extracted [18].

When a sample experiences a strong static magnetic field (B_0), all the spins of the paramagnetic nuclei orient in the same direction as the B_0 with the Larmor angular frequency of

$$\omega_0 = B_0 \times \gamma, \quad \text{(Eq. 1.1)}$$

where γ is the nuclear gyromagnetic ratio that is specific to the atom (e.g., for H nuclei (proton) γ is about 42.58, and for C it is about 10.71) [19]. The Larmor frequency is defined as the rate of the magnetic moment orientation changes in the presence of an external magnetic field and is specific to each nucleus. ^1H and ^{13}C are the most NMR active nuclei in organic chemistry resulting in H NMR spectroscopy and C NMR spectroscopy. Due to the abundance of the ^1H, which is 99.9%, the H NMR spectroscopy, also called as proton NMR spectroscopy is widely used [20]–[24]. In this spectroscopy, spectrum shifts indicate the neighboring atoms of Hydrogen, and the amplitude of the signal shows the number of corresponding atoms. For this aim, the Larmor frequency of the H NMR spectroscopy device is set by the Larmor frequency of the ^1H.

During the excitation mode, the RF signal responsible for creating the weak oscillating magnetic field (B_1) is generated at the Larmor frequency. B_1, which is perpendicular to B_0, changes the sample's nucleus spins orientation and rotates them with an angular velocity of

$$\omega_1 = \gamma \times B_1. \quad \text{(Eq. 1.2)}$$

Therefore, at the end of the excitation mode (assuming it takes τ seconds), sample's nucleus spins obtain an angle of

$$\theta = \gamma \times B_1 \times \tau, \qquad \text{(Eq. 1.3)}$$

with respect to their first orientations.

When the excitation is over, meaning $B_1 = 0$ (relaxation mode), all the sample spins go back to their equilibrium positions (because of B_0) and due to this reorientation, they emit the energy they have obtained during excitation [25]. As a result, based on the Faraday's law, if an inductor (i.e., the detection coil) is placed in the proximity of the sample, an electromotive force will be induced in it. This energy is then transduced by the detection coil, and the resulted signal, which is called free induction decay (FID), is sent to a spectrometer to extract its frequency-domain spectral information [26]. The shifts in the spectrum due to the local environment and spin-to-spin coupling carries information on the spins distance and provides information on the molecular structure [19]. The amplitude of the FID signal can be calculated by

$$S = \omega_0 \times M_0 \times V_s \times B_u, \qquad \text{(Eq. 1.4)}$$

in which V_s is sample volume, B_u is field per unite current of the detection coil, and M_0 is the macroscopic magnetization created by B_0 and calculated as

$$M_0 = \frac{N_s (I+1) I \gamma^2 \hbar^2 B_0}{3 K_B T}, \qquad \text{(Eq. 1.5)}$$

where N_s is the density of spins, I is the nuclear spin, ħ is the Plank constant, K_B is the Boltzman constant, and T is the sample temperature. Macroscopic magnetization is the net magnetic moment per unit of a sample in a given region, caused by all the individual microscopic nuclear magnetic moments [27][28].

To achieve a higher spectral resolution at the output, a stronger FID is required. The spectral resolution determines the maximum number of spectral peaks that the spectrometer can resolve. Better spectral resolution results in a more precise sample structure extraction, since the shifts in the frequency spectrum are more distinguishable. Based on *Eq.* 1.4, the FID magnitude is directly proportional to B_u. As a result, the NMR spectroscopy spectral resolution could be improved by making the detection coil's B_u stronger and more uniform. Aside from B_u, a larger B_0 and sample volume, as well as a lower temperature, all increase the magnitude of the FID [16][29]. In parallel with improving FID magnitude, a high signal-to-noise ratio (SNR) is required to achieve better resolution. Higher SNR means having stronger signal with less noise. So, increasing SNR leads to receiving a bigger signal with lower noise by the spectrometer, enable us to detect weak signals coming different atoms in a sample, therefore improving the resolution. Device spin sensitivity is another contributing factor in the spectral resolution [30]. The spin sensitivity is defined as the number of spins generating a SNR of one, i.e., $\frac{N_0}{SNR} = \frac{N_S V_S}{SNR}$ ($\frac{spins}{\sqrt{Hz}}$) [31]. A coil with lower sensitivity achieves higher SNR with smaller number of spins. This is particularly useful for spectroscopy with low concentration samples, such as biological macromolecules spectroscopy analysis [30].

A commercially-available NMR spectroscopy system is shown in Figure 1-2. In this picture, all the described components are housed in the cylindrical shape structure. The main contributing factor in the size of the device is the need for a giant magnet to generate the huge static magnetic field. Other factors effecting the size of the device are a cooling chamber of liquid Helium and liquid Nitrogen for maintaining the device temperature, an

external shimming circuit consisting of coils for adjusting the magnetic field homogeneity to parts per billion (ppb) in a volume of a few cubic centimeter, and an external tuning

Figure 1-2 An actual NMR spectroscopy system [32]

circuit containing of capacitors and resistors for setting the frequency and output impedance of the NMR system.

1.2.1. Signal-to-Noise Ratio (SNR)

A known drawback of NMR spectroscopy is its inherent SNR [33]. It is calculated as

$$SNR = (M_0 V_s \omega_0)\left(\eta \frac{U\left(\frac{B_i}{i}\right)}{\sqrt{4K_B\,(T_c R_c + T_s R_s)\Delta f}}\right), \qquad \text{(Eq. 1.6)}$$

where ŋ is the filling factor, U is the detection coil magnetic field uniformity, B_i is the detection coil magnetic field, i is the detection coil current, R_c is the detection coil

resistance, Δf is the bandwidth of the readout circuitry, and $T_s R_s$ is related to the sample thermal noise.

Among the parameters in Eq. 1.6, some are constants (e.g., T_c, K_B) and some are out of our control (e.g., T_s). As expected from our discussion in the previous section, increasing B_0 (hence, M_0) will improve SNR. This is the main reason that NMR systems are physically massive [27]. With a small sample size, sample thermal noise is negligible. As a result, although SNR is directly proportional to the sample volume, but it also inversely related to the sample noise. Subsequently, increasing sample size does not necessarily improve SNR. Moreover, small sample size means consuming less material, both in terms of sample and the associated miniaturized detection coil, which as discussed in the next part improves the NMR spectroscopy system. Also, small amount of sample is advantageous when dealing with low concentration samples such as biological analysis. Eq 1.6 also suggest that decreasing the detection coil resistance (R_c) improves the SNR. Moreover, increasing the detection coil magnetic field uniformity enhances the SNR. Considering this and the importance of B_u as discussed previously, indicate the importance of the detection coil's design geometry.

1.2.2. Spin Sensitivity

Another crucial factor in spectral resolution, besides SNR, is the spin sensitivity of the NMR spectroscopy system. As mentioned above, spin sensitivity is defined as the number of spins generating SNR of one. Lower spin sensitivity means that fewer number of sample spins are required to generate the desired SNR. There are several ways to enhance this sensitivity. Similar to SNR, sensitivity is improved by increasing static magnetic field

magnitude (B_0). This approach requires giant bulky magnet. The other approach is using dynamic nuclear polarization in which the sample is doped with a stable paramagnetic polarizing agent, then irradiated with microwaves to transfer the high polarization in the electron spin reservoir to the nuclei under scrutiny [15], [29], [34]–[36]. This method enhances the overall sensitivity of the system by altering the energy levels of the nuclei of interest rather than manipulating the NMR device itself, and subsequently is not a part of NMR device design workflow [37].

Another way to improve sensitivity is employing precise and efficient sensory probe and system [38]. This could be achieved in different ways such as optimizing detection coil size, optimizing detection coil parameters to reach a better quality factor, and boosting the performance of the electronic readout circuit connected to the detection coil in terms of input-referred noise, amplification gain, and bandwidth. More specifically, the spin sensitivity is directly related to the coil's diameter. For a solenoid coil with a diameter less than one mm, the coil sensitivity, defined as the magnetic field generated by the coil when a unit current is flown in, is calculated by

$$\frac{B_i}{i} = \frac{\mu n}{d_{coil}\sqrt{1+\frac{h_{coil}}{d_{coil}}}}, \qquad \text{(Eq 1.7)}$$

where μ is the permeability of the sample, n is the number of turns, d_{coil} is the coil diameter, and h_{coil} is the coil length. The coil resistance when $n \gg 1$ and $d_{coil} \gg \delta$ (skin depth) is calculated by

$$R_c = \frac{3\rho n^2 d_{coil}\xi}{2h_{coil}\delta}, \qquad \text{(Eq 1.8)}$$

where δ accounts for proximity effects from neighboring wires. *Eq.* 1.6, *Eq.* 1.7, and *Eq.* 1.8 leads to the following equation [39].

$$Spin\ sensitivity \propto \frac{N_S V_S}{SNR} \propto \frac{d_{coil}}{\gamma W^{\frac{7}{4}}}, \qquad \text{(Eq 1.9)}$$

Based on the *Eq* 1.9, the spin sensitivity is directly proportional to the coil diameter, meaning that smaller coils outperform their larger counterparts in terms of spin sensitivity.

It should be noted that if only the detection coil size decreases while maintaining the sample size, the filling factor would be degraded. Filling factor is a measure of the fraction of the coil volume occupied by the sample [27]. The best sensitivity can be achieved by a filling factor of one in which the sample and the detection coil are of the same size, so the coil only detects magnetic field variations due to the sample, while no part of the sample being outside of the coil's sensitivity region. If filling factor is smaller than one (i.e., sample is smaller than the coil) in addition to sample, air and other material above the coil affect the results, and if it is bigger than one (i.e., sample is bigger than the coil), only the part of the sample which is above the coil and exposed to its magnetic field could be detected. So, aside from the coil, sample should be downsized as well.

Besides the obvious benefit of reducing the required material, another advantage of shrinking the detection coil size is the fact that it allows for using an array of NMR probes in one system, which enables increasing the NMR spectroscopy system's overall throughput. Consequently, in the recent years, using micrometer-scale coils (a.k.a. μcoils)- for NMR applications have been widely investigated [40]–[44]. Olson *et al* have shown that the NMR sensitivity could be improved by using a high-resolution μcoil and (beside

consuming less sample) in comparison with a $5\,mm$ conventional NMR coil ($5\,nL$ compared to $278\,\mu L$) [45]. Grimes *et al.* presented that using a detection µcoil enhances the NMR sensitivity for metabolomic studies compared to $5\,mm$ conventional NMR coil [40]. Fratila *et al.* showed that using a µcoil integrated on a microfluidic chip with a sample volume of $25\,nL$ can detect various nuclides in a wide range of Larmor frequencies from 61 to $400\,MHz$ [41]. Fugario *et al.* evaluated different planar µcoils on a fish egg and concluded that using a µcoil increases SNR compared to a $5\,mm$ standard coil. They also demonstrated that single-cell NMR would be feasible in the near future using planar µcoils , which has the potential to provide rich insight on individual cells [42].

1.3. NMR Spectroscopy Types

NMR spectroscopy systems could be categorized by the strength of the external magnetic field B_0 , as well as the frequency in which they operate, i.e., the Larmor angular frequency. Based on this categorization, three types of NMR spectroscopy systems exist. (1) High-Frequency NMR, (2) low-frequency NMR, and (3) zero-field NMR.

High-frequency NMR works in the range of $220-1000\,MHz$, and uses a very strong static big magnetic field ($B_0 = 5$ to $24\,T$) [26], [46]. Low-frequency NMR, which is also called benchtop NMR, works in the range of $21-100\,MHz$ and uses a static magnetic field in the order of 0.5 to $2\,T$ [47], [48]. The zero-field NMRs use the earth magnetic field only [35], [49]. The chemical shifts in the zero-field NMR spectrum are in the order of a few millihertz and usually are not resolved. High-frequency NMRs offer a better SNR than low-frequency ones, as predicted by the *Eq.* 1.6. This advantage comes at

the cost of a few major drawbacks/limitations including: (1) physical size of the system, due to the larger static magnetic field, (2) vulnerability of the giant magnet to physical and chemical properties of the environment and requiring high-technology material and techniques for maintaining the magnet properties, (3) requiring more complex spectroscopy readout systems due to operating at higher frequencies, (4) higher cost (both for the development and maintenance).

Given the pros and cons of both low-frequency and high-frequency NMR, and the trade-off between frequency and system size/complexity, choosing high-frequency NMR at the cost of higher system complexity is justifiable whenever high SNR NMR spectroscopy is desired. Especially, in the case of high-throughput NMR devices, high SNR outweighs the importance of the size, price, and complexity of the design. For example, in a 100-probe NMR spectroscopy device, the cost, size, and design complexity of the device vary slightly with a 1-probe NMR system. On the other hand, a 100-probe device enables the simultaneous analysis of 100 samples in a single run, resulting in saving time and cost considerably. Accordingly, in this project, a high frequency NMR spectroscopy is preferred over the low frequency one.

1.4. Conventional NMR spectroscopy Systems

The overall structure of an NMR spectroscopy system was introduced in section 1.2. In addition to the coils and magnets that were discussed in the last few sections, the system also has a tuning and shimming circuitry mainly consisting of capacitive parts to set the detection coil-capacitor resonance frequency to the Larmor frequency while matching the NMR device output impedance to a $50\,\Omega$ coaxial cable connected to the spectrometer.

Typically, the sample is inserted from the top of the shielded NMR system, while the probe (i.e., the detection coil and shimming/tuning circuitry), pulse generator, and spectrometer connections are routed through the bottom outlet.

In the conventional NMR spectroscopy systems, discrete passive probes are used. These probes include one millimeter-scale RF detection coil, and a passive tuning and matching circuitry. The detection coil size varies for different works reported in literature, with $5mm$ being the most common one. Despite their simple structure which makes them suitable for various applications, these probes have a few practical limitations, especially when we want to increase the number of detection coils to achieve higher NMR spectroscopy throughput. The first challenge is finding discrete electronics components for the tuning and matching circuit with no or little ferromagnetic property, so that the magnetic field has a minimal effect on their functionality, and also, they have minimum influence on the uniformity of the magnetic field [50]. Another practical issue is the physical size of the discrete components attached to these probes, which makes the probe placement in the highly-constrained space inside the NMR system challenging [51]. These challenges might not be as serious when using a single probe, but the main issue with the discrete passive probes is their scalability. For boosting the throughput of the NMR spectroscopy system, meaning scaling a single-probe to multi-probe system for enabling capability of multi-sample per run, the physical size and ferromagnetic components of these probes become the main bottleneck. This is perhaps the main reason that the currently-available NMR systems do not offer many-probe high-throughput spectroscopy. So, these limitations led designers to move to the next generation of probes.

1.5. CMOS-based NMR Spectroscopy

To overcome the drawbacks of discrete probes design and implementation of the detection coil and its associated electronic components using a standard complementary metal-oxide-semiconductor (CMOS) process has been investigated over the past two decades [29], [50], [52]–[54]. A CMOS-based implementation allows for significant coil size reduction, which, as discussed previously, results in decreasing the sample size, hence a better filling factor, which leads to a higher SNR [27]. More importantly, by using the CMOS technology (especially, the sub-micron nodes), we can integrate thousands of passive and active electronic components on a mm-scale silicon die, allowing us to miniaturize the entire readout circuit (as well as additional optional signal processing blocks). The small form factor of the electronic blocks also has the benefit of minimizing the magnetic field distortion. Additionally, fabrication of an integrated CMOS-based probe, particularly in large quantities, requires significantly lower cost and time [50].

Another advantage of an integrated CMOS-based solution is the design flexibility and the degree of freedom it offers in designing the matching and tuning, and readout circuits. By leveraging the sub-μm size of integrated switches (i.e., transistors) in CMOS technology, the electronic circuits used for any of the above tasks could be dynamically tuned after fabrication, to account for any changes caused by process, voltage, or temperature variations. Therefore, unlike the discrete design where the components are fixed and there is very little room for design flexibility, using integrated circuits allow for post-fabrication tuning and adjustment of almost all circuits. Similarly, the low cost of

additional active components allows for employing structures to isolate the impedance matching and frequency tuning blocks as shown in [48].

Driven by this, several studies have been conducted on the feasibility of utilizing CMOS integrated circuits for low- and high frequency NMR probes (also called as NMR receiver). Figure 1-3 shows a typical implementation of CMOS-based probes in a conventional NMR spectroscopy system. As shown, the main difference with a conventional NMR spectroscopy system is the detection coil and its associated circuit, and the giant static magnetic field and the excitation signal generation are the same. The figure also shows that the sample holder and the microchip (hosting the detection µcoil and all electronic circuits) mounted on a printed circuit board (PCB) and are sandwiched together, and are placed in the system's excitation coil. All connections to the external spectrometer are made through the PCB. It should be noted that in some designs, only the electronic circuits are integrated on a CMOS chip which is connected to an off-chip µcoil [29], [48], while in some others both the coil and the electronics are implemented on-chip [52], [53], [55].

While an off-chip µcoil allows for higher number of turns, thus a better quality factor, a fully on-chip solution (i.e., both coil and the circuits implemented on the chip) is generally preferred mainly because (1) the detection coil and the circuits are connected together through a short on-chip conductor, therefore, the signal attenuation before reaching the readout circuit is significantly smaller compared to the case with an off-chip detection coil where the signal has to travel through the packaging and I/O connection

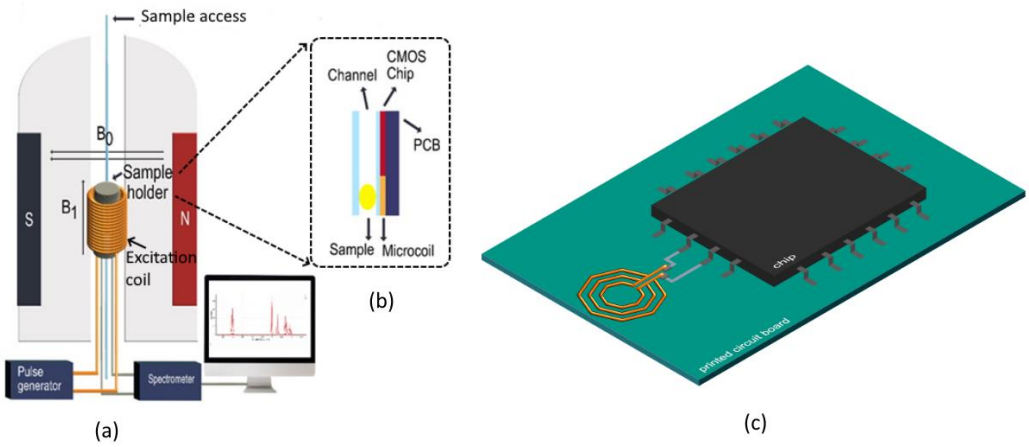

Figure 1-3 NMR spectroscopy system. (a) A simplified block diagram of the NMR spectroscopy system. (b) Cross-view illustration of the inside of the sample-holder consisting of the µcoil, CMOS chip, and sample. (c) An isometric view of the off-chip µcoil connected to the CMOS chip.

before reaching the first stage of readout circuitry; (2) in the solution with an off-chip coil, the bond wires connecting the on-chip circuitry to the detection coil are long enough to affect the detection coil's effective inductance and negatively impact its sensitivity and SNR [53].

The first fully integrated NMR probe was reported in 2001 by Boero *et al.* with the NMR system that had a static magnetic field (B_0) in the range of $0.7\text{-}7\,T$. The size of detection coil was in the range of a few millimeters, hence not considered a µcoil. There was also no internal matching circuitry in this design [29]. The spectral resolution was reported to be unacceptable for most of the spectroscopic applications. Reducing electronic noise, improving the detection coil quality factor, and adding a matching circuitry were the proposed methods to improve the poor obtained resolution. The first fully integrated multi-channel system (i.e., multiple detection coils working in parallel) was introduced by Anders

Table 1-1 A comparison on CMOS NMR receivers

References	*Technology (μm)*	*Frequency (MHz)*	*On-chip blocks*	*#Channels*	*Spin sensitivity* $(\frac{Spin}{\sqrt{Hz}})$	*Area (mm × mm)*
[53]	0.13 IBM	300	Coil, Tuning cap, LNA, Mixer, IF amp	1	5×10^{14}	0.95 × 0.8
[52]	0.35	300	Coil, Tuning cap, LNA, Mixer, AF amp	1	-	1.2 × 0.85
[54]	0.13 2P6M	300	Coil, LNA, mixer, AF amp, amp (+transmitter)	1	1.5×10^{13}	1 × 1
[31]	0.13 IBM	300	Tuning cap, LNA, Mixer, IF amp, Driver stage	1	2×10^{13}	350 × 450
[48]	0.8 AMS	85.13	Tuning cap, LNA, Buffer	1	-	> 1 × 1
[55]	0.35 AMS	300	Coil, Tuning cap, LNA, Buffer	8	10^{15}	1 × 2
[29]	0.5	350	Coil, RF amp, mixer, AF amp	1	-	10 × 10
[56]	0.13	300	Coil, Tuning cap, LNA	3	-	1 × 2
[50]	0.13	300	Coil, LNA, Mixer, AF amp	1	-	1.1 × 1.1

et al. for parallel spectroscopy at $300\ MHz$ [55]. The matching circuitry was implemented on-chip in this work and the detection coil occupied an area of $520\ \mu m \times 520\ \mu m$.

While earlier NMR systems used separate coils for excitation and detection, in recent years, there have been several reports of using the same coil for both tasks [50], [54]. In these systems, the electronic circuits connected to the coil should be capable of both RF signal transmission and reception by using switches. Since the coil changes its role during

the operation, a switch connects it to the applicable circuitry designed for RF transmission (Tx) and reception (Rx). In designing the mode-switching circuit, it is critical that the Rx and Tx circuit blocks are fully isolated from each other [54].

Table 1.1 summarizes the NMR systems with an on-chip integrated probe implemented with a wide range of coil sizes, technologies, and frequency of operation.

1.6. Motivations

There is a never-ending effort by the NMR spectroscopy system manufacturers to improve their technology's throughput and SNR. As explained in this chapter, this requires (1) better magnets to create the strongest possible static field (B_0), and (2) integrating as many NMR receivers (i.e., coil + readout circuitry) in one system as possible. A stronger B_0 translates into a higher Larmor frequency. It is also well known that the quality factor of sub-mm-scale coils increases with increasing frequency [57], [58]. In other words, by increasing the frequency of resonance, a physically smaller coil can yield the same desired quality factor. Both these points suggest that increasing the NMR spectroscopy's throughput is contingent on the development of an end-to-end procedure for the design and performance optimization of NMR receivers at a high frequency in the UHF band.

1.7. Objectives and challenges

The objective of this thesis is to present an end-to-end design procedure for an integrated high-throughput high-frequency NMR spectroscopy receiver. This is done by design and optimization of all the components in the NMR spectroscopy receiver, including the µcoil and the integrated read-out circuitry. For this purpose, the µcoil is designed and optimized

considering all the performance metrics such as SNR, spin sensitivity, quality factor, inductance, resistance, coil sensitivity, filling factor, and magnetic field uniformity. For the read-out circuit to be scalable, the adaptability of the tunning circuit to different µcoils and frequencies is considered. Moreover, the low noise amplifier is designed to achieve the required gain, bandwidth and noise performance, while requiring the lowest power consumption and area to maximize the throughput of the NMR spectroscopy.

This integrated NMR receiver is designed for a commercially-available $500\ MHz$ NMR spectroscopy device (Bruker), but it provides a platform for scaling the NMR receiver to higher frequencies. Although high-frequency NMR spectroscopy has higher sensitivity, the associated circuitry is more complicated. Besides more complex circuitry, in higher frequency, parasitic elements play a major role and should be taken into account. Moreover, to the best of our knowledge, all of the studies in the CMOS NMR are done in $300\ MHz$ and lower frequencies, and this is the first NMR CMOS receiver working in $500\ MHz$.

In the next chapter, the detection µcoil design, optimizations, and simulation results are presented. In chapter 3, the front-end circuitry, its system and circuit level designs, layout and post layout simulations and results are described. Finally, chapter 4 includes a conclusion of the work, contributions, the immediate next steps as well as long-term future directions for this research.

Chapter 2

Design and Optimization of an On-chip Detection µcoil

As described in the previous chapter, an integrated NMR system consists of two main parts: (1) An RF detection µcoil which operates as the electrical transducer, and (2) a readout circuit for amplifying the signal received from the µcoil before passing it on to the spectrometer. Each part plays an important role in achieving a high-sensitivity high-SNR NMR spectroscopy and should be individually optimized. In this chapter, the role of the µcoil and the design methods used to optimize the structure for achieving highest NMR spectroscopy performance are discussed. The design, implementation, and simulation results of the readout circuitry are presented in the next chapter.

2.1. Desired Specification

As previously mentioned, having a micrometer-scale detection coil (µcoil) is desired for highly-sensitive high-throughput mass-limited NMR systems [59]. On the other hand, a smaller coil and, and as a result a smaller sample, causes a lower voltage to be induced on the coil when it is exposed to a magnetic field, as analytically shown in *Eq* 1.4. To mitigate

this problem, a higher sensitivity of the coil is required. Sensitivity is defined as the magnetic field generated by the coil when a unit current is flown in it, and is calculated as,

$$B_u = \frac{B_i}{i} \qquad \text{(Eq 2.1)}$$

as shown in Eq 2.2 (same as Eq. 1.6 in Chapter 1, but the sample's thermal noise is neglected in this equation due to the small sample consumption in µcoil probe.), the NMR spectroscopy's SNR is dependent on several parameters that are grouped into three sections. The first section which is related to the static magnetic field's strength and the sample's volume was discussed in the previous chapter. The third group is related to the noise contributed by the readout circuitry and will be discussed in the next chapter. The second group of parameters are all dependent on the detection coil and its structure (as labeled in the equation). Here, ŋ represents the filling factor, U is the coil magnetic field uniformity, $\frac{Bi}{i}$ represents the coil sensitivity, Tc is the coil temperature, and R_c is the coil resistance.

$$SNR = (M_0 V_s \omega_0)\left(\eta \frac{U\left(\frac{B_i}{i}\right)}{\sqrt{T_c R_c}}\right)\left(\frac{1}{\sqrt{4K\Delta f}}\right). \qquad \text{(Eq 2.2)}$$

Magnet & sample-related Coil-related Front-end-circuit-related

Consequently, having a high SNR, highly sensitive NMR receiver requires an optimal µcoil design.

2.1.1. Coil Impedance and Quality Factor

Based on the *Eq* 2.2, SNR is proportional to the coil resistance (R_c), which represents the noise generated by the coil. Therefore, decreasing R_c improves the overall NMR system's

SNR. Accordingly, the coil's quality factor (Q), which is defined as "the ratio of the coil reactance to its resistance" and calculated by *Eq* 2.3,

$$Q = \omega \frac{L}{R_c}, \quad \text{(Eq 2.3)}$$

should be maximized. In Eq. 2.3, ω ($\frac{Rad}{S}$) is the frequency, and L is the inductance. A high Q indicates a high SNR from another perspective as well. Since the coil's inductance is directly related to B_i, as shown in *Eq* 2.4).

$$L = \frac{1}{\mu_0} \int_{all\ space} B_i^2 dv, \quad \text{(Eq 2.4)}$$

where μ_0 is the vacuum permeability, increasing L (which is embedded in Q) indirectly improves the SNR. Both above points argue that for a higher overall system SNR, the coil must be designed to have the maximum quality factor. Having high quality factor also relaxes the design requirements for the readout circuitry as will be discussed in the next chapter.

2.1.2. Strength and Uniformity of the Coil's Magnetic Field

According to *Eq* 1.4, the coil's magnetic field (B_u) is a contributing factor in the FID signal amplitude, and a stronger magnetic field improves the FID signal, hence the SNR and sensitivity. This motivates for a larger coil inductance, which is against what we have argued previously (i.e., having a smaller coil being desired for high sensitivity, filling factor, etc.). The trade-off suggests that the coil area can be made smaller as long as it still generates an FID signal that is above the input-referred noise level of the readout electronic circuit. While the minimum inductance for the detection coil is reported in some works in

the literature, there are works such as [60], [61], where authors have decided to report the generated magnetic field by the coil for 1 A current, which is in the range of 10 to 14 mT. This number can be converted to the inductance using Eq 2.4.

The uniformity of the magnetic field produced by the µcoil is another important factor that affects SNR and sensitivity (shown by "U" in the Eq 2.2). Despite its importance and its direct impact on the system's SNR, we could not find any quantitative metric in the literature that is used to specify the design requirement for this parameter. Nonetheless, as discussed later in this chapter, we have considered uniformity in our coil design as one of the key parameters and tried to maximize it for our final design

2.2. Important Performance Metrics in Coil Optimization

Different types of µcoils are being used as detection coil in NMR systems including solenoid µcoils [47], [62]–[64], planar µcoils [26], [46], [60], [65]–[71], stripline µcoils, Helmholtz µcoils, and microslots [64], [72]–[75]. Among these, planar ones are compatible with the CMOS technology. More recent sub-micron CMOS technology nodes have been shown to be suitable for fabrication of planar µcoils in small sizes (i.e., sub-mm radius) by offering several metal layers with different thicknesses. Using multiple metal for physical implementation of the µcoil allows for limiting the coil area and perimeter to fixed desired values while increasing the inductance and quality factor by adding more spiral routings in a second or third layer. Moreover, fabrication of the spiral planar µcoil is the most straightforward amongst all type of coils, because of a layer-by-layer fabrication technique which is the typical method in MEMS fabrication [76].

On the other hand, planar µcoils have lower sensitivity and SNR compared to solenoid µcoils due to their high resistance and low quality factor [64], [65]. Although planar µcoils have less sensitivity than solenoid ones, it is shown that they can be used in the NMR system with high SNR. In 1997, J. E. Stocker showed that a multi-turn square planar µcoil can be used for high SNR by optimizing the turns and sample position [68]. Knowing that planar µcoils are capable of having high quality factor, are compatible with CMOS technology, and are easier to fabricate and consume less space have drawn attention to planar µcoils in recent years [42], [47], [65], [68], [69], [77], [78]

Increasing the metal thickness is one way to increase the planar µcoil's quality factor [79], [80]. This is the main reason that planar coils are generally implemented in top metal layers which have higher thickness. Other reasons that lower metal layers are not used for coil implementation is their inherent higher metal resistivity, which causes Q reduction, and the fact that lower metal layers are typically used for active circuit implementation and their routings. While thickness is more or less fixed in CMOS technologies by the fabrication house, there are other geometrical parameters of the coil that we could optimize during the design to achieve high quality factor. This includes the number of turns, the width of each turn, the shape of the µcoil, the material, the distance between the turns, the number of layers, and how the turns in different layers connect to each other.

2.2.1. µcoil Architecture

As mentioned, CMOS technology offers multi-layers µcoils. The number of metal layers varies depending on the technology; for example, in $0.35\text{-}\mu m$ Austria Micro System

(AMS) technology which we have used in this work, only four metal layers can be used, while in TSMC 0.13-μm, 8 layers are available. Depending on how many layers are used for coil implementation, the number of turns in each layer, and how these turns and layers are connected together, different categories/architectures of on-chip spiral µcoils could be implemented, as described next.

2.2.1.1. Serial Stacked Coil (SSC)

In this category, as shown in Figure 2-1(a), multi-turn spiral structures are routed in different layers and then connected to each other in a series fashion using vias (a via is a conductive connector that is used in CMOS technology to connect structures in different metal layers together). Due to their structure, they allow for many turns (hence, high inductance), but suffer from high resistance. For a µcoil implemented in m layers, each with n turns, the total resistance is simply calculated as (ignoring the via resistances)

$$R_c = \sum_{J=1}^{m} \sum_{i=1}^{n} R_{j,i} \qquad \text{(Eq 2.5)}$$

2.2.1.2. Differential Stacked Coil (DSC)

In this category, as shown in Figure 2-1(b), multi-turn spiral structures are routed in different layers but divided in half. In each layer, the half-spiral is connected to the layer above in a series fashion using vias. Unlike SSC, this structure has the benefit of low resistance due to its parallel structure [81]. For a µcoil implemented in m layers, each with n turns, the total resistance is simply calculated as (ignoring the via resistances)

$$R_c = \sum_{J=1}^{m} \left(\sum_{i=1}^{n} \frac{1}{R_{j,i}}\right)^{-1} \qquad \text{(Eq 2.6)}$$

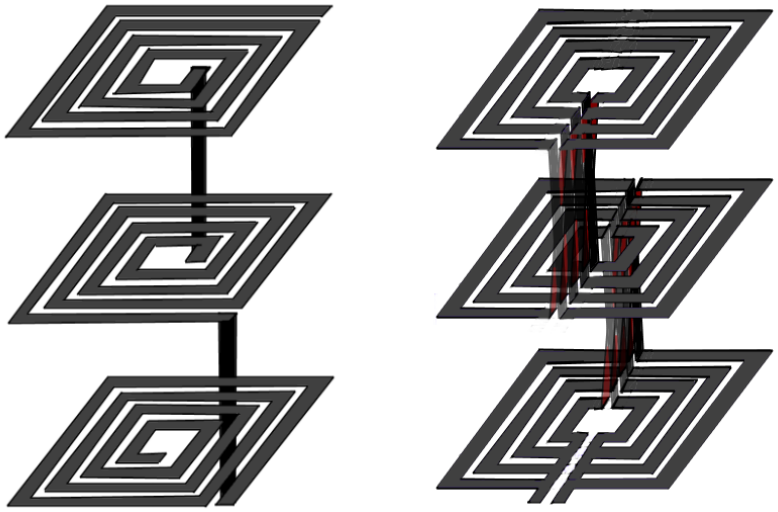

Figure 2-1 4-turns 3-layers square (a) SSC, and (b) DSC µcoils.

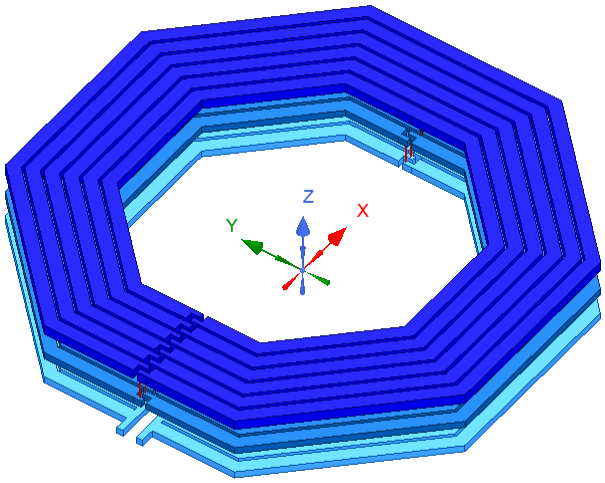

Figure 2-2 A DSC coil structure in HFSS software [82]**.**

According to *Eq* 2.5 and 2.6, DSC µcoils have lower resistance compared to SSC ones for the same inductance, hence have higher quality factor. Therefore, in this work, we have used DSC structure to achieve a higher quality factor.

2.2.2. Geometrical Shape

The circular-shaped coils create one of the most uniform magnetic field among other coil shapes because of their rotational symmetry [83]. However, in the CMOS technology, it is not possible to have an exact curve, hence implementing a perfectly circular µcoil is not feasible. With a square-shaped coil being simplest for design and fabrication, and worst in terms of uniformity, and a circular coil being the opposite, a polygon shape with > 4 sides seems to be the best option. instead, the coil should have a polygon shape. The more sides a polygon has, the more similar it is to the circular coil and the magnetic field would be more uniform. In this thesis, an octagonal shape is chosen so a better magnetic field uniformity could be achieved while the limitations of CMOS in terms of layout precision are also met.

2.2.3. Material and Thickness

Some materials are NMR compatible, meaning that they barely manipulate NMR output signals due to their intrinsic characteristics. Magnetic susceptibility of a material is the most critical property for determining whether it is NMR friendly or not, which defines the degree of the magnetization of a material in response to an applied magnetic field [84]. Any mismatch in the magnetic susceptibilities of the materials used in the NMR system leads to a broader NMR signals in the spectrum, hence decreasing the spectral resolution

and SNR. Among all the materials, copper (Cu) is one of the best options to be used in an NMR system, with the magnetic susceptibility of -9.63×10^{-6} [85].

As discussed earlier, thick metal layers in the µcoil increase the SNR [79]. So, besides material, the thickness of metal layers should be considered when choosing the CMOS technology node for on-chip implementation, since the layers thickness is technology specific. For standard CMOS, once the technology node is chosen, the material and thickness of the metal layers in a CMOS chip are fixed (certain special non-standard processes might offer special post fabrication metallization options). So, the best CMOS technology is the one that offers thick copper metal layers. A slightly less important factor for choosing the technology is the number of available metal layers. More layers give the opportunity of having more configurations for the µcoil in the limited space with more turns which could be beneficial. However, as will be shown, we typically end up using only the top 2-to-3 layers for coil implementation and adding more layers beyond these numbers tends to have a negative impact on the Q.

Among the CMOS technologies offered by the Canadian Microsystem Corp (CMC), the best available technology was the AMS 0.35-µm. This technology node offers four metal layers, which includes a thick Aluminum top layer.

2.2.4. Configurations and Number of Layer

Considering that four metal layers are available, 15 different configurations could be imagined for coil implementation, i.e., $\binom{4}{1} + \binom{4}{2} + \binom{4}{3} + \binom{4}{4} = 15$ where $\binom{4}{m}$ is the m-combination of 4 layers.

As will be described in next few subsections, based on our ANSYS High-Frequency Structure Simulator (HFSS) simulations [82], the best overall configuration is achieved by using the second, third, and fourth layers (from the bottom) of the 0.35-μm CMOS chip.

2.2.4.1. μCoil Layer-stack Configuration Optimization Using HFSS

For choosing the best configuration of the layers, all the 15 configurations were simulated using Ansys HFSS and based on the achieved quality factor, magnetic field strength and uniformity the best one has been chosen. For this purpose, fifteen 4-turns octagonal μcoils with inner diameter (ID) of $500\ \mu m$, wire width (WW) of $20\ \mu m$, and turn distance (TD) of $20\ \mu m$ with different layers (based on each layer's average thickness given by the CMC) has been simulated. Then their Q, $B_{z,mean}$ (magnetic field strength in z axis), $\frac{B}{\sqrt{R_c}}$ (proportional to the SNR), L, and $B_{z,mean}$'s STD (standard deviation to show magnetic field uniformity) are compared in our operating point, i.e., $500\ MHz$, since the accessible NMR system is working in this frequency. Additionally, the magnetic field uniformity in 4 different heights from the coil's surface are compared. Simulation results from a subset of the 15 possible combinations that had better overall performance are presented in Table 2.1 and figures 2-3 to 2-6 below.

Table 2-1 Comparing the electrical characteristics of µcoils developed using different layer configurations

Layer configurations	$B_{1Z-mean}$ *(T)*	R_c *(Ω)*	$\frac{B_{1Z-mean}}{\sqrt{R_c}}$	*Q*	*L (nH)*	$B_{z,mean}$*'s STD*
1-layer (4)	0.00286	1.2910	0.0025	3.1867	0.6547	0.2182
2-layer (1,4)	0.00786	3.2307	0.00437	5.0850	2.6146	0.3022
2-layer (3,4)	0.00618	3.4808	0.0033	4.8212	2.6709	0.3105
2-layer (2,4)	0.00907	3.2910	0.0049	5.0429	2.6413	0.3081
3-layer (1,2,4)	0.01024	7.2252	0.0038	5.4970	6.3212	0.3146
3-layer (2,3,4)	0.01051	7.4743	0.0038	5.4929	6.5342	0.3269
4-layer	0.01810	18.3064	0.0042	5.0062	14.5859	0.3653

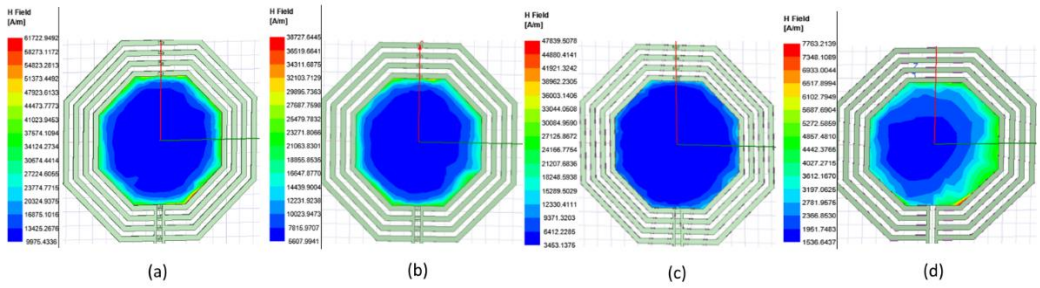

Figure 2-3 Magnetic field strength in the XY plane on the Surface: (a) Four-layer, (b) Three-layer (2,3,4), (c) two-layer (3,4), and (d) one-layer (4).

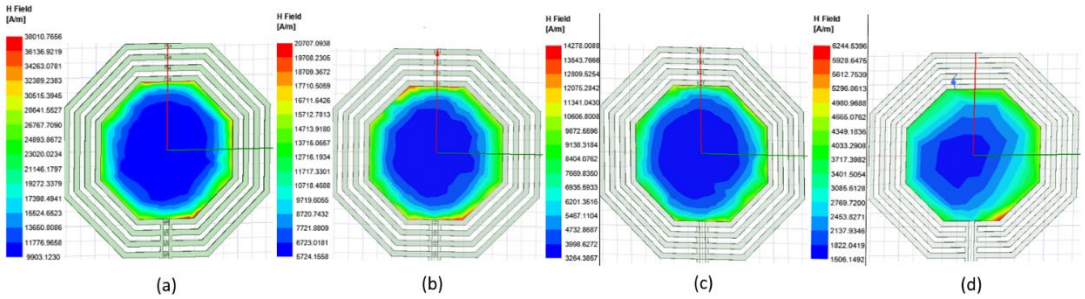

Figure 2-4 Magnetic field strength in the XY plane 2030nm above the Surface: (a) Four-layer, (b) Three-layer (2,3,4), (c) two-layer (3,4), and (d) one-layer (4).

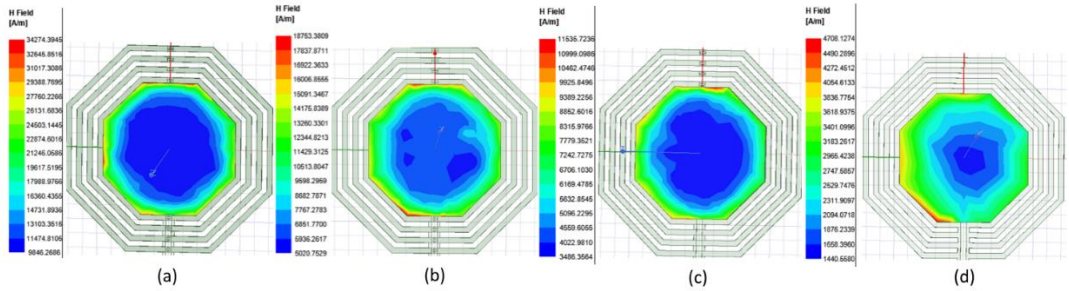

Figure 2-5 Magnetic field strength in the XY plane 3030nm above the Surface: (a) Four-layer, (b) Three-layer (2,3,4), (c) two-layer (3,4), and (d) one-layer (4).

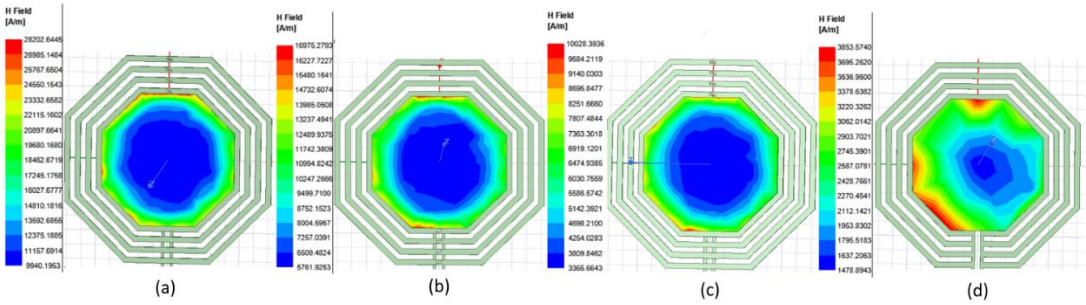

Figure 2-6 Magnetic field strength in the XY plane 4030nm above the Surface: (a) Four-layer, (b) Three-layer (2,3,4), (c) two-layer (3,4), and (d) one-layer (4).

Based on these simulation results, the best configuration for quality factor is using layers 2,3, and 4 while the best magnetic uniformity is for using 4-layers, but it is only

slightly higher than the 3-layers (2,3,4). This means that a 3-layer coil implemented in the second, third, and fourth layers is the best option overall.

2.2.5. Number of Turns

As shown in the equation below, the coil inductance, and subsequently the magnetic field, is directly proportional to the number of turns,

$$L = N\frac{\Phi}{I}. \qquad \text{(Eq 2.7)}$$

Increasing the µcoil's number of turns also leads to a more uniform magnetic field, of course, at the cost of higher ohmic impedance. Based on the *Eq* 2.3, a higher L and R_c increases and decreases the Q, respectively. This suggests that there is an optimum number of turns for the best quality factor for each coil.

2.2.5.1. Optimizing the µcoil's Number of Turns in Each Layer

One of the most important limitations of µcoil design is its size. The entire integrated NMR probe (i.e., the µcoil and the readout electronic circuits all integrated on a chip) is placed in a small cylinder in the NMR device, so the space is limited for the whole chip. Having a multi-channel receiver in such a small space limits the area even more for each channel's µcoil. Here, considering practical limitations of the NMR systems used by our collaborator (Bruker), we decided for the total area of about $500\ \mu m \times 500\ \mu m$ should be dedicated to each µcoil.

Based on this area limitation, the number of turns, the inner diameter, the trace width, and the distance between traces are all inter-dependent and restricted. For optimizing the number of turns the same approach as in section 2.2.4.1, is taken. Based on

Table 2-2 Comparing different number of turns in one layer

#Turns	$H_{1Z-mean}$ *(A/M)*	$B_{1Z-mean}$ *(T)*	R_c *(Ω)*	$\frac{B_{1Z-mean}}{\sqrt{R_c}}$	*Q*	*L (nH)*	*STD*
3	10185.9298	0.0128	4.6961	0.005906	3.8881	2.9060	0.4109
4	10077.0077	0.012663	4.4531	0.006001	4.1438	2.9368	0.4418
5	9845.7649	0.012372	4.2089	0.006031	4.3228	2.8957	0.3968
6	9806.8877	0.012323	4.1276	0.006066	4.4230	2.9102	0.3888
7	9886.8749	0.012424	4.3182	0.005979	4.3194	2.9686	0.3942
8	9898.5754	0.012439	4.5124	0.005856	4.1716	2.9960	0.3908
9	10012.4987	0.012582	4.7966	0.005745	3.9935	3.0487	0.3955
10	10154.4517	0.01276	4.8730	0.00578	3.9921	3.0961	0.3830

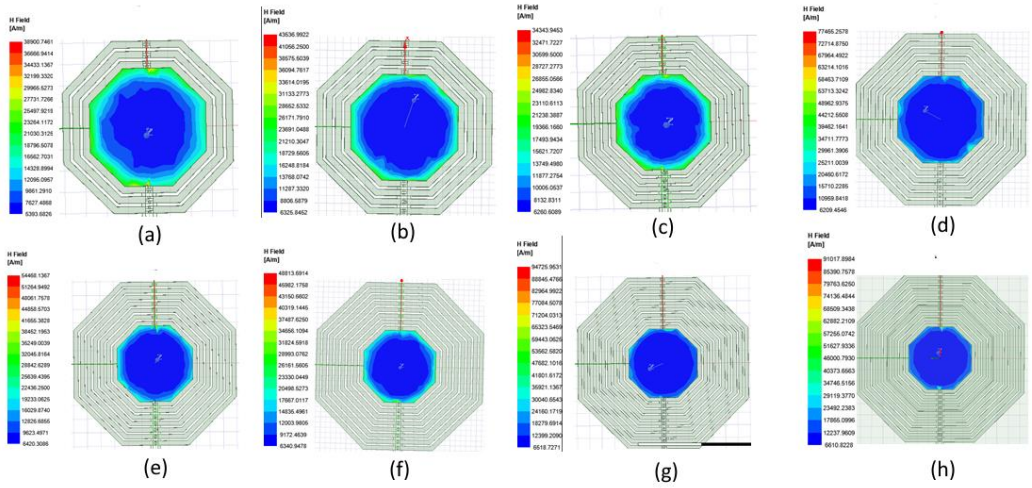

Figure 2-7 Magnetic field strength in the XY plane 2030nm from the surface for different number of turns. (a) 3-turns. (b) 4-turns. (c) 5-turns. (d) 6-turns. (e) 7-turns. (f) 8-turns. (g) 9-turns. (h) 10-turns.

these results presented in Table 2.2 and Figure 2-7, the best number of turns in each layer for our area restriction is 6.

2.2.6. Inner Diameter, Trace Width, and Spacing

The inner diameter, the traces width and spacing should also be optimized for the best overall performance, considering CMOS layout rules and the available space. For this purpose, we conducted numerous simulations by sweeping over different ranges and steps for inner diameter, wire width, and turn's distance considering the total space of $500\ \mu m \times 500\ \mu m$ with 6 turns, and CMOS design rules.

First, the inner diameter is set, which cannot be larger than 150 μm due to the space limitation. Based on the result, a larger inner dimeter leads to a higher quality factor, so the inner diameter of $150\ \mu m$ was chosen. Considering the total area of $500\ \mu m \times 500\ \mu m$, with inner diameter of $150\ \mu m$, and 6 turns, wire width and turns distance were even more constrained. For optimizing these two parameters, initially a large range with big steps were chosen and simulated, then based on the results, range and steps were gradually narrowed down and eventually after many iterations the best WW and TD were selected, which are $14\ \mu m$ and 5 μm, respectively.

Among the discussed parameters, besides inner diameter which also defines the coil area and is limited, number and configuration of the layers have the most influence on the results for several reasons. First, it contributes to the total number of turns hence assist in having higher number of turns in a limited space. Secondly, the layer configuration determines layers effect on each other and the distance among them. Finally, the chosen layers also lead to the metal thickness in each layer which as described, is one of the most effective parameters to improve the μcoil quality factor.

2.3. Characterization of the Final µcoil Design

Based on the HFSS simulations, we found a 6-turn octagonal µcoil with wire width of 14 µm and turn distance of 5 μm to be the most optimized design for the outer diameter of 518 µm and using the second, third and fourth layers of the CMOS chip. The final µcoil structure is shown in Figure 2-8.

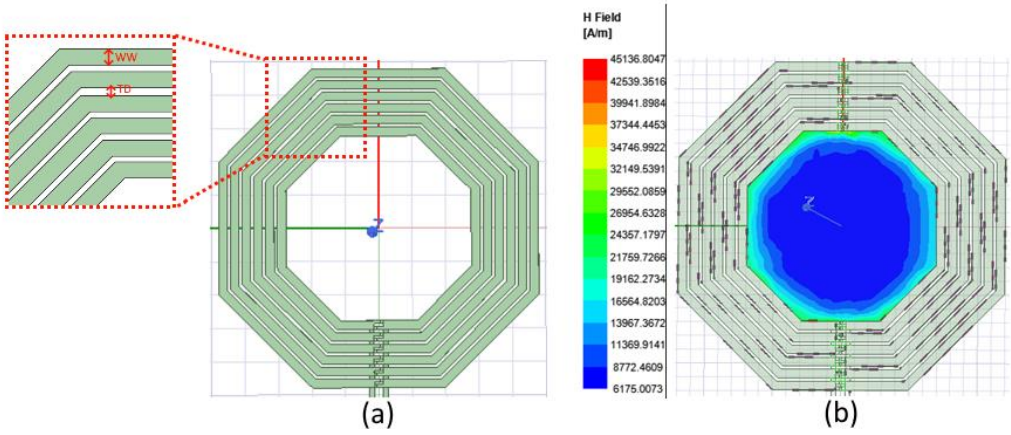

Figure 2-8 (a) Top view of the designed µcoil in HFSS, showing wire width and turn distance. (b) Simulated magnetic field strength in the XY plane 2030 nm above the Surface.

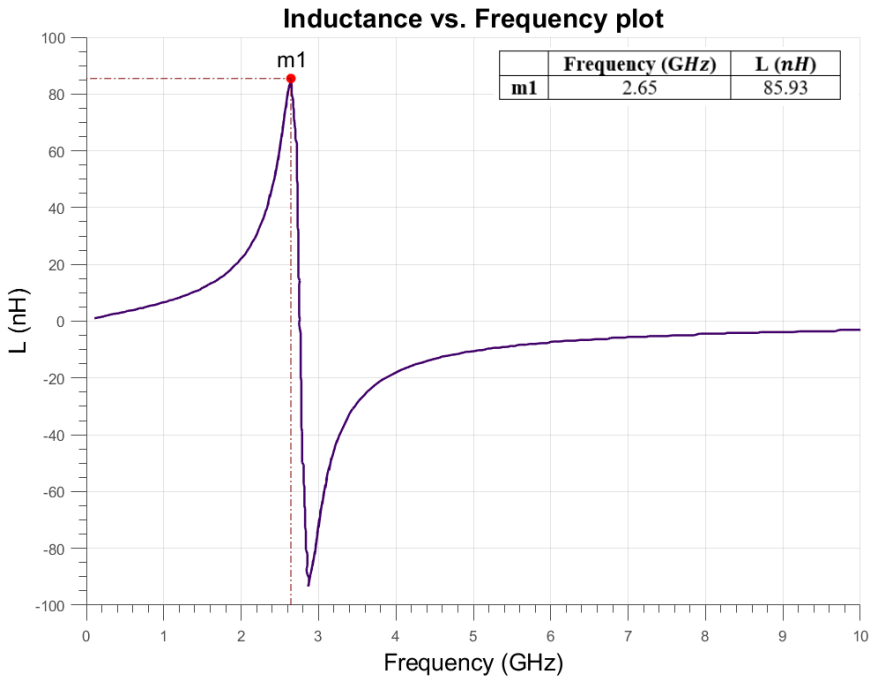

Figure 2-9 Inductance vs frequency diagram of the µcoil.

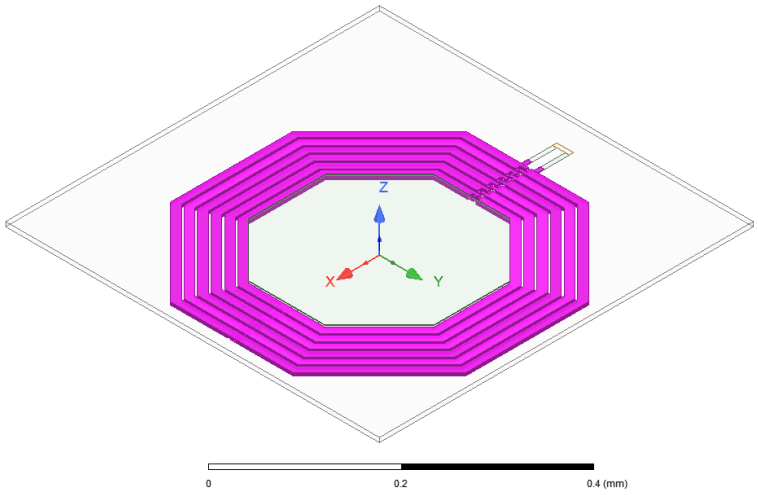

Figure 2-10 The Isometric-view of the coil (pink) and the substrate (light gray).

As shown in Figure 2-9, the designed µcoil's self-resonance frequency (SRF) is 2.6457 GHz, which is higher than our operation point (i.e., 500 MHz, but considering

shifts in the NMR spectrum a bandwidth of 100 MHz is of interest of our collaborator. So, the operation frequency is in the range of 450 – 550 MHz). This means that for our targeted range of frequency, the coil will indeed work as an inductor. self-resonance frequency is the frequency at which the parasitic capacitance of the coil resonates with the inductance of the coil creating a very large impedance in a way that the coil works as an open circuit. The quality factor, the inductance, and the resistance of the designed µcoil is measured to be 4.7188, 2.902 nH, and 3.8642 Ω, respectively, and the generated magnetic field is 12.46 mT at 1 A current.

2.4. µcoil Optimization Considering the Substrate

In the previous section the µcoil was simulated and optimized in the air. But, in real-world CMOS technology metal layers are placed on top of a semiconductor substrate which is typically Crystalline silicon (c-Si). Additionally, as part of the fabrication process, on top of the top metal layer, one or two passivation layers (e.g., oxide or nitride) are formed, mainly to protect the internal semiconductor devices.

Here the designed µcoil is simulated in the new environment to find the effect of this change in the final results. The substrate has a thickness of 4705 nm and is considered to be Silicon dioxide. Also, two passivation layers with the thickness of 1000 nm and 1030 nm respectively is added to the simulations.

As it is shown above, the changes are considerable. So, for having more accurate results in real world, all the optimization described in sections 2.2.4.1, 2.2.5.1, and 2.26 were repeated considering metal layers on the substrate and passivation layers.

Based on the simulation results, a 6-turn octagonal µcoil with the width of 12.5 μm and distance of 3 μm is the optimal design for an outer diameter of 480 µm and using the second, third and fourth layers of the CMOS chip. The final µcoil structure is shown in Figure 2-11.

Table 2-3 The effect of adding substrate on the µcoil performance

Properties	*Q*	*L (nH)*	*R (Ω)*
Coil in the air	4.7188	2.9021	3.8642
Coil in the substrate	4.2229	3.2095	4.7753
Changes from air	-0.4959	+0.3074	+0.9111
Changes from air (%)	-10.5090	+10.5923	23.5780

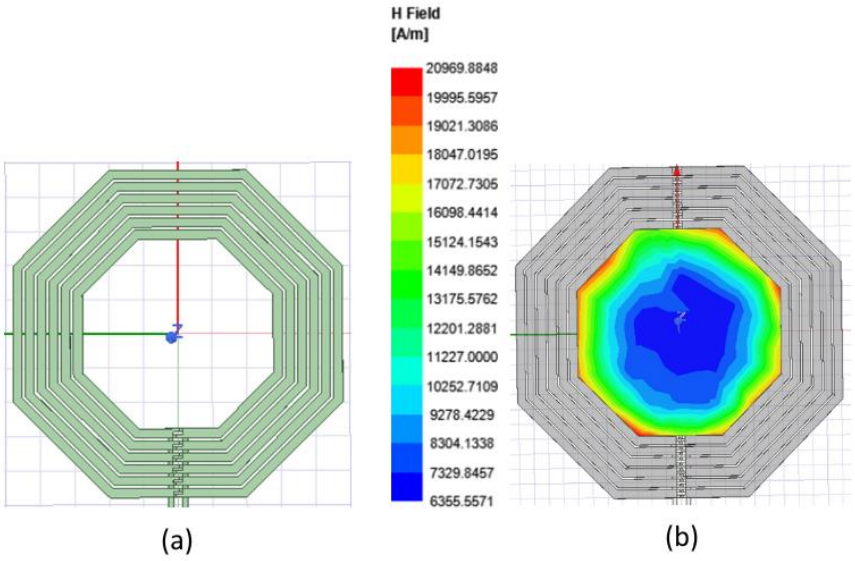

Figure 2-11 (a) Top view of the designed µcoil in HFSS with a wire width of 12.5µm, and turn's distance of 3µm. (b) Simulated magnetic field strength in the XY plane 2030 nm above the Surface.

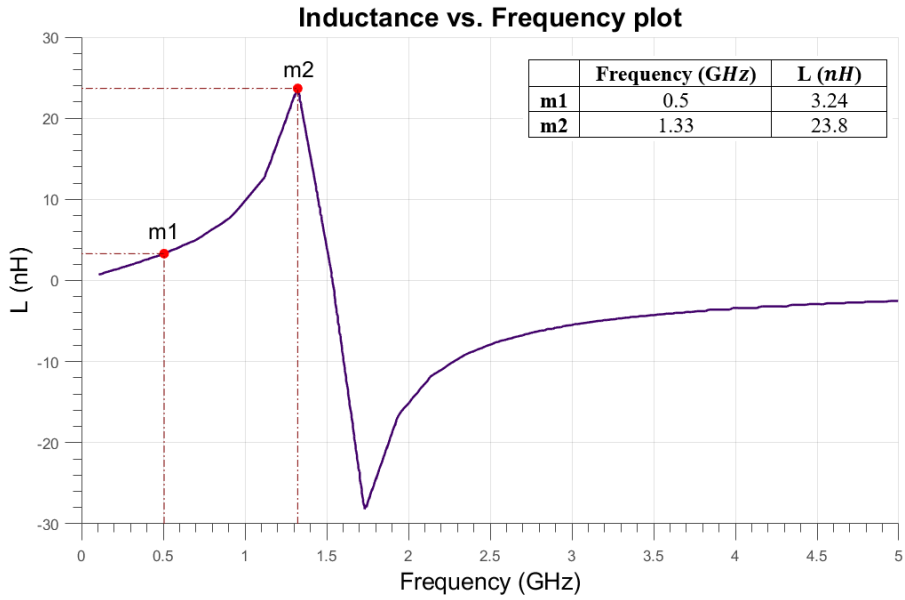

Figure 2-12 Inductance vs frequency diagram of the µcoil.

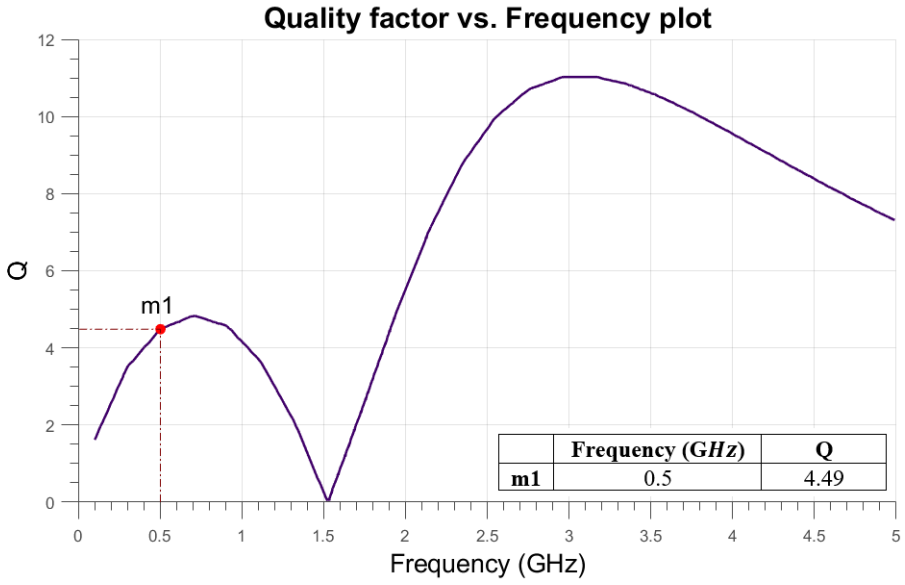

Figure 2-13 Quality factor vs frequency diagram of the µcoil.

The updated µcoil self-resonance frequency (SRF) is $1.325\ GHz$, which is higher than our operation range of frequency.

Also, as shown in Figure 2-13, the highest Q in the inductive range is achieved near $500MHz$. Although the highest Q has not been achieved at exact 500 MHz, but this quality factor is the biggest quality factor achieved at 500 MHz among all the combinations for the coil (even those with the highest Q peak at 500 MHz). The highest peak is above SRF, where the coil has a capacitive behavior rather than an inductance one.

The quality factor, inductance, and resistance of the designed µcoil are 4.4701, $3.1726\ nH$, and $4.4594\ \Omega$, respectively, and the generated magnetic field is $12.84\ mT$ at $1\ A$ current.

2.5. µcoil Simulation in the Presence of a Sample

For having more realistic results, the µcoil (with substrate) is simulated in the presence of distilled water sample. The sample is modeled as a half sphere shape with a diameter equal to the µcoil's outer diameter, as shown in Figure 2-14.

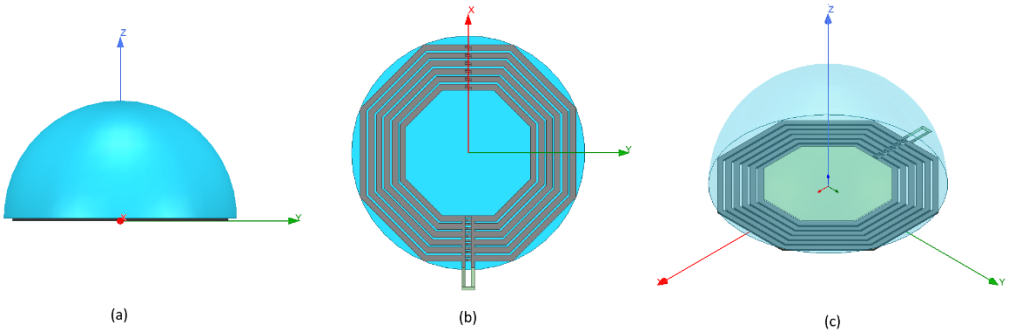

Figure 2-14 (a) 3D cross-view, (b) button-view, and (c) isometric-view of the coil (gray) and the sample (blue).

Table 2-4 The effect of adding sample on the µcoil electrical characteristics

Properties	***Q***	***L (nH)***	***R (Ω)***
Coil + substrate	4.4701	3.1726	4.4594
Coil + substrate + sample	4.2822	3.2304	4.7400
Changes	-0.1879	0.0578	0.2806
Changes (%)	-4.2035	1.8218	6.2923

Table 2-5 The effect of sample diameter variations on the µcoil characteristics

OD (um)	*L (nH)*	*Q*	*R (Ω)*
300	3.2302	4.2848	4.7368
320	3.2302	4.2738	4.7489
340	3.2305	4.2816	4.7408
360	3.2302	4.2821	4.7398
380	3.2305	4.2785	4.7442
400	3.2299	4.2783	4.7435
420	3.2316	4.2832	4.7406
440	3.2315	4.2753	4.7491
460	3.2293	4.2829	4.7376
480	3.2304	4.2822	4.7400

The effect of adding and varying the sample on the µcoil characteristics are shown in the Table 2.4 and 2.5, respectively. As expected, the changes are not significant. Also, changes in characteristics are partly due to the limited precision of the HFSS software, even with the highest mesh configuration.

2.6. Comparison with the State-of-the-art

Table 2.6 compares the final result of the described µcoil optimization with the state-of-the-art integrated CMOS-based µcoils.

Figure 2-15 shows the final µcoil design laid out in Cadence (using the AMS 0.35um kit) for integration with the readout electronic circuits described in the next chapter.

A summary of the electrical and physical characteristics of the coil are also reported in the figure.

Table 2-6 CMOS µcoils

References	*F (MHz)*	*Area (µm × µm)*	*Shape*	*#Turns*	*Q*	*Technology (µm)*	*Uniformity*
[53]	300	345 × 345	Square	10	3.5	0.13	N/M
[54]	300	-	Octagonal	22	<1.69	0.13	N/M
[31]	300	345 × 345	Square	10	-	0.13	N/M
[55][52]	300	520 × 520	Square	-	8	0.35	N/M
[29]	350	2000 × 2000	2-squares	12	3.25	0.5	N/M
Our work	500	480 × 480	Octagonal	18	4.47	0.35	Yes

N/M = Not mentioned

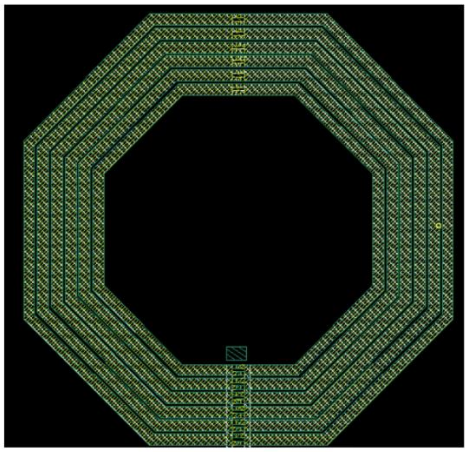

Inner diameter	150 µm
Outer diameter	480 µm
#Turns	6
Turn width	12.5 µm
Turn distance	3 µm
Shape	Octagonal
Structure	DSC
#Layer	3

Quality factor	4.47
Inductance	3.17 *nH*
Resistance	4.46 Ω
Self-resonance frequency	1.32 *GHz*
Magnetic field	12.84 *mT*

Figure 2-15 µCoil layout in the cadence and its characteristics.

Chapter 3

Design and Characterization of the Readout Circuit

To complete the NMR spectroscopy probe, the µcoil designed and optimized in the previous chapter must be connected to a readout circuit. The purpose of this circuit is to amplify the induced signal from the µcoil to increase its signal to noise ratio before passing it to the spectrometer. Despite all the optimization steps taken in the µcoil design, the induced signal on the coil is still quite weak (i.e., low SNR). Without signal amplification (i.e. direct connection of the µcoil to the spectrometer via a cable), the signal will be drawn in the noise and interference coupled onto it along the way. The readout circuit may have different sub-circuits depending on the specific system requirements, but the common elements in most of the studies are (1) a tuning and matching circuitry, (2) a low noise amplifier (LNA), (3) an interfacing block between the readout circuit and the spectrometer. This block in some systems is a down-converting mixer circuit [31], [52]–[54], and in some other designs is a high-frequency wideband voltage buffer with an output impedance

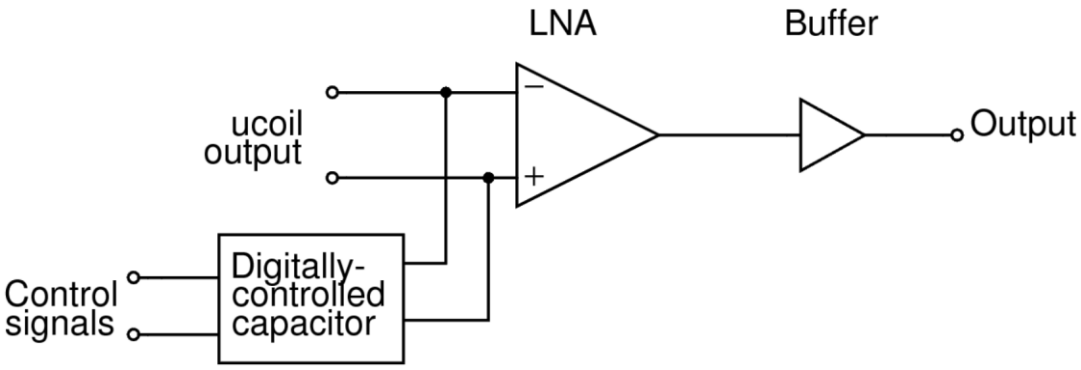

Figure 3-1 Readout Front-end circuit system-level design.

matched to the resistance seen looking into the coaxial cable between the spectrometer and the miniature NMR probe [48][55].

In this work, our circuit consists of a tuning circuitry, an LNA, and a buffer and is designed to support two NMR receiving channels. The system-level design of the front-end circuit is shown in Figure 3-1.

In this design, the first channel includes the readout circuitry and an on-chip µcoil which is the one that is designed in chapter 2, and the second channel only consists of the readout circuitry and works with an off-chip µcoil. This allows for (i) testing the readout circuit separate from the coil, (ii) comparing the results of an on-chip coil with and off-chip one, (iii) multi-channel testing.

The front-end circuit for the first channel is designed based on the µcoil describe in chapter 2, and for the second channel is designed based on an off-chip µcoil designed by our collaborator's group (Dr. A. Simpson, NMR facility, University of Toronto) but is also

flexile to be used by other off-chip µcoils that their physical and electrical characteristics are not significantly different from their µcoil.

In this chapter, we will present the design, physical layout development, and post-layout simulation results for both these channels.

3.1. Tuning and Matching Circuitry

The µcoil is connected to an LNA, through a tuning circuitry that sets the operation frequency. Having a parallel capacitor (C) that resonates with the µcoil inductance (L) at the Larmor frequency f_0, along with an LNA with infinite input resistance would minimize the noise figure of the µcoil and LNA together [25]. The noise figure of a component shows the SNR degradation caused by the component itself in the signal chain. So, for the LNA to have a small noise figure, and less effect on the input signal due to its noise, it should have lower input referred noise power spectral density ($\frac{\overline{v_{n,L}^2}}{\Delta f}$) than the coil's noise power spectral density ($\frac{\overline{v_{n,c}^2}}{\Delta f}$) after travelling through the tunning circuit. Here, we consider for the tunning circuit to be a passive network with voltage transfer function of $H(\omega)$ which includes the LNA's input impedance (Z_{LNA}) effect, and α is defined as $\alpha = H(\omega_L)$. If the passive network's noise is negligible, the coil 's noise power spectral density after travelling through it is measured by $\alpha^2 \frac{\overline{v_{n,c}^2}}{\Delta f}$. As described, if $\alpha^2 \frac{\overline{v_{n,c}^2}}{\Delta f} \gg \frac{\overline{v_{n,L}^2}}{\Delta f}$, the LNA noise figure is small. Therefore, maximizing the passing network gain (α) and minimizing LNA input referred noise power spectral density both improve the noise figure, hence improving the SNR. The latter will be discussed in section 3.2, while the former is related

to the tuning circuit. For increasing α, an LNA with infinite input impedance is required since any finite impedance will lower the voltage at the passive network output (we should keep in mind that Z_{LNA} is considered in $H(\omega)$). For the passive network, a capacitive network is considered as shown in Figure 3-2 (b). In this network for maximizing the gain, C_2 is set to be infinite to be short circuited. C_1 should be set in a way to maximize α which is calculated as $\alpha(C_1)=\frac{1}{\sqrt{(1-LC_1\omega^2)^2+(C_1R_c\omega)^2}}$. For doing so, $C_1 = \frac{1}{L\omega^2}$, meaning that the maximize gain is achieved when a parallel capacitor, which resonates with the coil at the Larmor frequency, is connected in parallel to a LNA with infinite input impedance, hence improves the noise figure and SNR [25]. This LC network resonates at,

$$f = \frac{1}{2\pi\sqrt{LC}}, \qquad \text{(Eq 3.1)}$$

Another advantage of the tuning and matching circuit is pre-amplifying the signal at the resonance frequency before reaching the LNA. Even though the main purpose of this circuit is not voltage amplification, it acts as an amplifier (even with typically a small gain) at the resonance frequency with a gain approximately equal to the Q. So, improving the μcoil's quality factor will increase the preamplifier gain. To describe this quantitatively, a simplified model for the non-ideal LC network is considered (Figure 3-2 (a)), which includes the μcoil resistance.

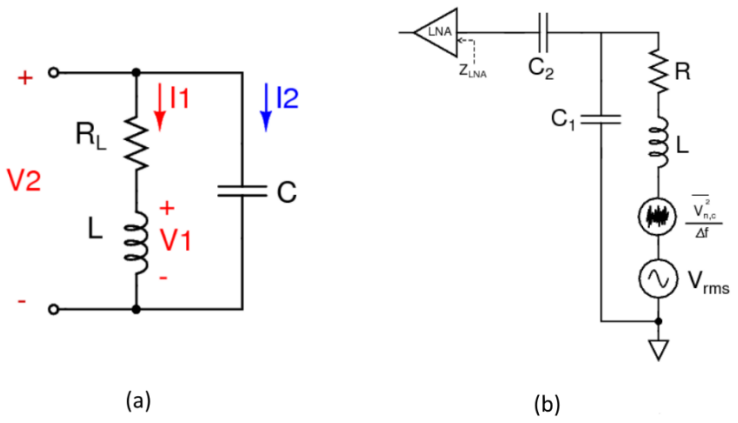

Figure 3-2 (a) Simplified non-ideal coil and tuning capacitor circuit, since capacitor has much higher quality factor, it is assumed to be ideal with no resistance. (b) Coil and LNA connection using a passive capacitive network.

For the tuning capacitor to resonate at the Larmor frequency, $500\ MHz$ in our case,

$$Z_t = \frac{R(1-LC\omega^2)+RCL\omega^2}{(1-LC\omega^2)^2+(RC\omega)^2} + J\frac{(1-LC\omega^2)\times\omega L - R^2C\omega}{(1-LC\omega^2)^2+(RC\omega)^2}. \quad \text{(Eq 3.2)}$$

Where Z_t is the equivalent circuit impedance. For this circuit to resonant at the frequency of ω, the imaginary part of the Z_t should be zero at ω. Hence the required capacitor calculated by,

$$C = \frac{L}{(L\omega)^2+{R_c}^2}. \quad \text{(Eq 3.3)}$$

Also based on this, voltage amplification gain for this non-ideal LC network, which is the voltage across the terminals of the circuit in Figure 3-2(a) over the voltage across the coil is calculated as,

$$V2 = V1 + RI2 + j\omega LI2, \quad \text{(Eq 3.4)}$$

$$I2 = \frac{V2-V1}{R+j\omega L}, \quad \text{(Eq 3.5)}$$

Combining *Eq* 3.4 and 3.5, The voltage gain is calculated as,

$$A_v = \left|\frac{V2}{V1}\right| = \frac{1}{\sqrt{(1-LC\omega^2)^2+(CR_c\omega)^2}}. \quad \text{(Eq 3.6)}$$

In almost all the reported integrated CMOS NMR receivers, this tuning circuit is a fixed capacitor [52], [55], [56] , simply because the system is designed to work only for a single frequency for a single µcoil. In this work, instead of a constant capacitor, a variable capacitor is employed mainly because it makes the circuit compatible with different µcoils. So, this circuit could be used with various off-chip µcoils without needing an external tuning circuitry. Moreover, for a designed on-chip µcoil there are always differences between the pre- and post-fabricated µcoil characteristics, particularly, its inductance. Having an adjustable resonance capacitor allows for accounting for these variations as well as chip-to-chip variations.

The variable capacitor consists of a bank of binary-weighted capacitors, CMOS switches, and a digital controller. The schematic is shown in the Figure 3-3.

For the digital controller, a shift register circuit is used to minimize the number of input signals. This is to ensure that the number of wires that need to routed inside the NMR system are minimized. For the switches, an NMOS transistor is connected to each end of individual capacitors to make sure that the capacitor is completely disconnected from the inductor (i.e., no parasitic effects) and the output when needed. Since the capacitors are in parallel, the total capacitor is a simple algebraic sum of all the capacitors that their switches are on. For switch sizing, the most important criteria is minimization of the parasitic

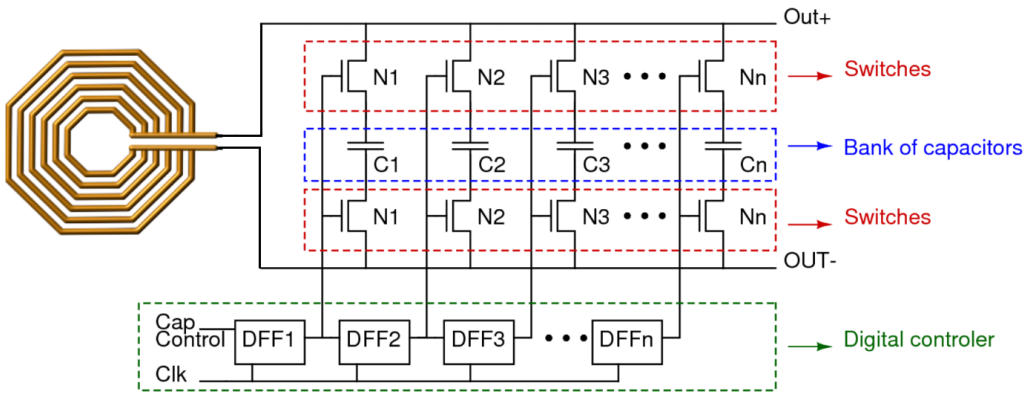

Figure 3-3 Variable capacitor schematic.

resistance of these switches as their speed is of least importance for our application (as we don't change their state during operation).

The range and step size of the capacitor bank are set based on the µcoil characteristics and *Eq* 3.3. Since the µcoils in the two channels are different and have different inductances and resistances, the variable capacitors for channels one and two are different from each other and should be designed based on their own µcoil. In setting the range, we considered the largest possible coil inductance variations after fabrication, and designed the capacitor bank in a way that the LC bank can always resonate at 500MHz. The step size (i.e., the LSB of the capacitor bank) was set based on the required spectral precision for the NMR spectroscopy.

3.1.1. Tuning Circuit Design for the First Channel (On-chip µCoil)

For the nominal inductance of the designed µcoil in chapter 2, the required capacitor to oscillate at the Larmor frequency of $500\ MHz$ is $26.61\ pF$ based on *Eq* 3.3.

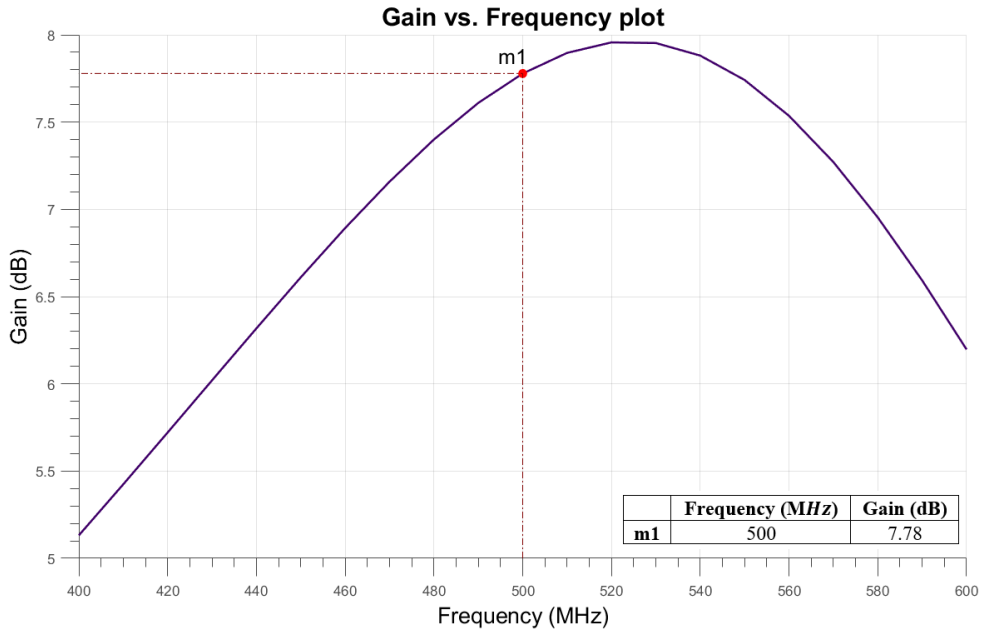

Figure 3-4 RLC network ac gain.

$$31.4159 \times 10^8 = \sqrt{\frac{1}{3.1726\times10^{-9}C} - \left(\frac{4.4594}{3.1726\times10^{-9}}\right)^2} \rightarrow C = 26.6096\, pF$$

Accordingly, based on the *Eq* 3.4, the voltage gain at 500 MHz will be 2.4485 or 7.7782 dB.

The circuit was also simulated (ac analysis) using Cadence Specter simulator and the voltage gain was confirmed as shown in Figure 3-4.

3.1.1.1. Desired characteristics and Design

For determining the variable capacitor range and steps, the post-fabrication and chip-to-chip variations should be considered. Since microchip fabrication foundries do not disclose the precise values for the metal thickness in each layer, the µcoil electrical characteristics

Table 3-1 µcoil's L and Q variation based on the CMOS layers' thickness changes

Variation	*L (nH)*	*Q*
Minimum	3.013875	3.536609
Maximum	3.453819	5.001528

described in Chapter 2 were calculated based on the "nominal" thickness values. However, the metal thickness variations could be significant and could change the µcoil's inductance and quality factor by a considerable amount. For this purpose, HFSS simulations were conducted, in which the CMOS metal layers thicknesses were changed (A total of 1764 different combinations were considered). Based on the results the minimum and maximum values for the L and Q are presented in Table 3.1.

For the lowest and highest µcoil's inductance and quality factor, the required capacitor value for the on-chip µcoil to resonates at the Larmor frequency is calculated based on the *Eq* 3.3 and is presented in table 3.2. Additionally, the variations in the sample dimeter is considered for obtaining the variable capacitor range and step size. For this purpose, different sample sizes, ranging from outer diameter of 300 µm (i.e., equal to µcoil inner diameter) to 480 µm (i.e., equal to µcoil outer diameter) were simulated in the HFSS. The desired capacitor for generating the Larmor frequency for the smallest and biggest sample is reported in Table 3.2. In this table, the fabrication variation and sample size effect on the µcoil properties, especially its inductance, and hence the range of the required capacitor for oscillating at the Larmor frequency is discussed.

Table 3-2 Capacitor variation based on the L, Q, and sample diameter changes

Properties	*C*	*C variation (pF)*	*C variation (%)*
Thickness (Lowest L)	28.0442	+1.4346	+5.3913
Thickness (Highest L and Q)	22.2276	-4.382	-16.4677
Thickness (Lowest Q)	28.7102	+2.1006	+7.8941
Sample (OD=480μm)	25.7481	-0.8615	-3.2375
Sample (OD=300μm)	25.7555	-0.8541	-3.2097

OD=Outer Diameter

Based on the Table 3.2, for designed on-chip micro-coil, a variable capacitor in the range of 20-30 pF is needed. To achieve a reasonable spectral precision, 128 fF is chosen for the step size. To limit the number of bits controlling the capacitor bank, and knowing that the smallest required capacitor will be approximately 20pF, we decided to build the capacitor bank using a large fixed capacitor in parallel with a binary-weighted adjustable bank. For this purpose, a constant 16 pF capacitor is made in parallel with a variable one that can generate a capacitance in the range of 1-14 pF. The variable part of the structure can generate a capacitor in the range of 128 fF to 8 pF.

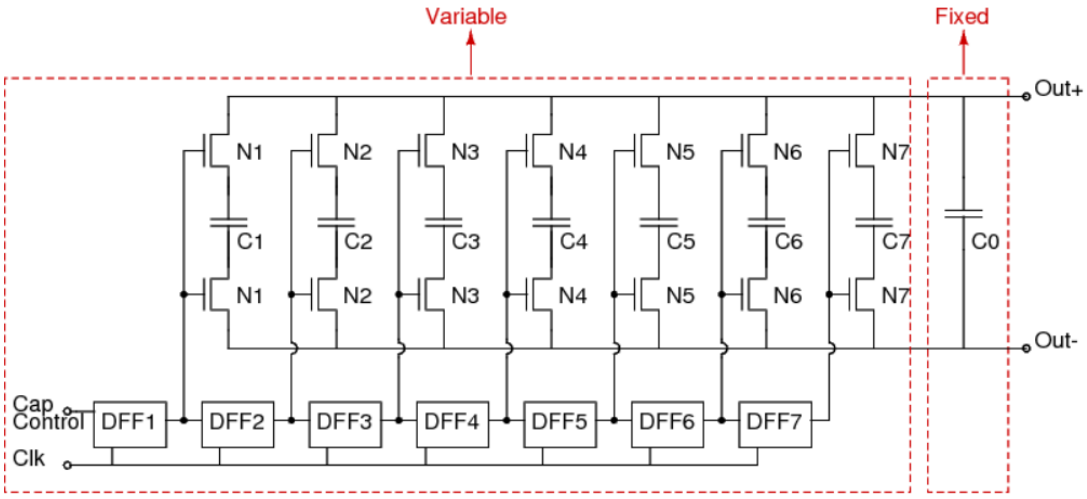

Figure 3-5 Channel one tuning circuit schematic.

3.1.1.2. Post Layout Simulations

The variable capacitor bank depicted in Figure 3.5 was implemented in AMS 0.35um CMOS process. The physical layout occupies an area of $320\ \mu m \times 270\ \mu m$ and is shown in the Figure 3-6.

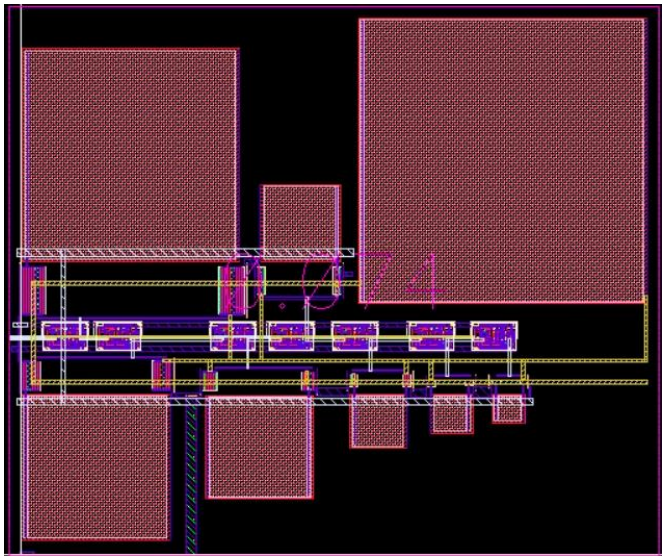

Figure 3-6 Channel one tuning circuitry layout.

Table 3-3 Channel one post layout simulation results

V7:V1 (digital output for turning switches off (0) and on (1))	***Expected C (pF)***	***Measured C (pF)***
0000000	16	16
1000000	24.16	24.16
0100000	20.08	20.08
0010000	18.04	18.05
0001000	17.02	17.03
0000100	16.51	16.51
0000010	16.25	16.25
0000001	16.12	16.12

The post layout simulation results at $500\ MHz$ are presented in the Table 3.3 (for a subset of possible digital inputs), which confirms that the desired variable capacitor has been achieved

3.1.2. Tuning Circuit Design for the Second Channel (without On-chip μcoil)

For this tuning circuitry, a range of $20\text{-}60\ pF$ and a step size of $0.5\ pF$ were requested by our collaborator researchers who were going to use this microchip for a biochemistry NMR application. To make the design future-proof, instead of the $20\text{-}60\ pF$, a range of $0\text{-}83\ pF$ was considered for our tuning circuit design. Therefore, unlike the circuit designed for the

on-chip µcoil, here we did not use a fixed capacitor in the structure. As depicted in Figure 3.7, the variable capacitor is constructed using a similar architecture as the circuit for the

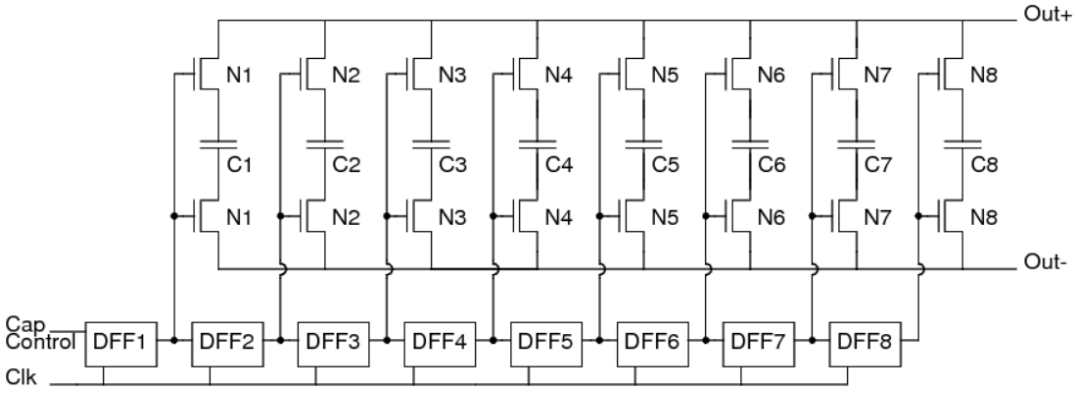

Figure 3-7 Channel two tuning circuit schematic.

first channel, but with an 8-bit capacitor bank capable of generating a capacitance from 0.5 pF to 32 pF.

3.1.2.1. Post Layout Simulations

Similar to the first channel, the tuning circuit shown in Figure 3.7 was implemented in AMS 0.35um CMOS process and the layout occupies an area of $460\ \mu m \times 490\ \mu m$ and is shown in the Figure 3-8.

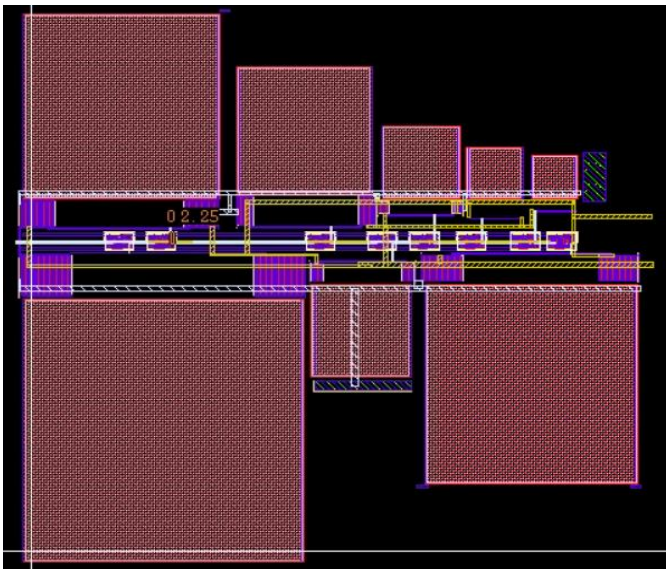

Figure 3-8 Channel two tuning circuitry layout.

The post layout simulation results at $500\,MHz$ are presented in Table 3.4. The results confirm that the desired variable capacitor is achieved. When all the switches are off, instead of a $0\,pF$ capacitance, an offset value of $0.92\,pF$ was observed, which was mainly due to the parasitic capacitances. It should be noted that this does not cause an issue as a capacitance smaller than 0.92pF is extremely unlikely to be required (it is only required if the real inductance of the µcoil is larger than $110\,nH$, which is 4300% different from the $2.5\,nH$ nominal value).

Table 3-4 Channel one post layout simulation results

V8: V1 (digital output for turning switches off (0) and on (1))	***Expected C (pF)***	***Measured C (pF)***
00000000	offset	0.92
10000000	32.92	32.92
01000000	16.92	16.91
00100000	8.92	8.92
00010000	4.92	4.91
00001000	2.92	2.92
00000100	1.92	1.91
00000010	1.42	1.41
00000001	20.92	20.96

3.2. Design of a Wideband Low Noise Amplifier (LNA)

As fully discussed in the previous chapters, despite several mentioned benefits, the miniature size of the detection coil in an NMR system results in the induced voltage (i.e., the FID) signal to be very small, in the range of hundreds of nanovolts to a few microvolts [19]. This demands for a low noise amplifier circuit directly connected to the coil to improve the FID's SNR before it gets drawn in noise or interference. Since the FID's frequency changes depending on the type and amount of the sample material, the amplifier should be functional for a wide range of frequencies centered around the resonance frequency (i.e., 500 MHz in this work).

A side outcome of this amplifier is to isolate the tuning capacitor from the output matching circuit [48]. To elaborate on this, the chosen tuning capacitor that generates the desired frequency with the µcoil inductance may affect the output impedance in a way that it will not match with the $50\ \Omega$ cable, which connects the coil to the spectrometer. This mismatch causes loss of signal energy while traveling from the coil to the spectrometer through the cable. On the other hand, if the capacitor is set to match the µcoil impedance to the cable it may cause the receiver to go out of tune, hence, partial or complete loss of signal [48].

3.2.1. LNA Design Specifications

3.2.1.1. Input Referred Noise (IRN)

Perhaps the most important performance metric in the design of the LNA is its input-referred noise. As mentioned, the FID is quite weak and a small noise contribution by the amplifier could result in the signal being drawn in noise. So, instead of a common RF amplifier, a low-noise RF amplifier is required. Moreover, as mentioned in section 3.1 lowering the LNA input referred noise improves the LNA noise figure and increases the SNR. The maximum allowed IRN depends on several parameters including the static magnetic field (B_0) strength, the coil size and structure, the sample size, etc. (all mentioned in *Eq*. 2.2). However, according to our review of state-of-the-art CMOS NMR LNAs, an input referred noise power spectral density of approximately 1.5 $\frac{nV}{\sqrt{Hz}}$, seems to be an acceptable amount for integrated CMOS-based sub-mm-diameter µcoils operating at hundreds of MHz resonance frequency [29], [33], [48].

3.2.1.2. Bandwidth

The LNA should work at the Larmor frequency, so it's bandwidth should include the Larmor frequency which in our case is 500 MHz. In addition, since the FID's frequency is expected to be slightly deviated from the Larmor frequency, the amplifier should yield the same performance (i.e., noise, gain, etc.) for ±50 MHz centered around the resonance frequency (i.e., 450-550 MHz). To the best of our knowledge, all CMOS NMR receivers are designed for 300 MHz and below, and this is the first 500 MHz-CMOS NMR receiver compatible with the Bruker NMR system. The bandwidth is as important as IRN in our design.

3.2.1.3. Gain

The third most important LNA characteristic is its gain. It is not as important as the first two characteristics mentioned above, since it could be complemented by another amplification stage if needed. We have experimental data from our collaborators showing that NMR spectroscopy with desired SNR is performed using a discrete LNA (Model: ZX60-P103LN) with a voltage gain range of 18-20.3dB at 500 MHz. As a result, a voltage gain of 21 dB seems to be sufficient. Our review of the recent works reveals a voltage gain of 30 dB is comparable to the state-of-the-arts [29], [50], [52].

3.2.1.4. Size

Since the application-level target of this work is enabling high-throughput (i.e., many-channel) NMR spectroscopy, it is important that the on-chip implementation of the coil and the readout circuitry are done with the smallest area required. That being said,

considering the size of the on-chip coil and the capacitive bank used for tuning, the LNA is expected to take a very small portion of the total area for each NMR channel, hence, its area is not one of the major design criteria.

3.2.1.5. Power Consumption

Power consumption is not a major concern in the design of the LNA mainly due to the availability of a cooling system in the NMR device. From the sample's safety perspective, and according to the experimental observations provided by our collaborators, a power consumption of up to a few hundreds of milli-watts is acceptable. Nevertheless, considering that this circuit is designed with the idea of scaling it to hundreds/thousands of channels, we tried to minimize the power consumption while satisfying all other design requirements.

3.2.2. Design Methodology

As mentioned in the section 3.1, the LNA must have an infinite input impedance to minimize the noise [25], which can be met by using a common-source configuration for the first stage. The IRN of a common source amplifier is calculated as,

$$\overline{V_{n,in}^2} = 4KT(\gamma g_{m1}) \times (r_{o1})^2 \times \frac{1}{((g_{m1})(r_{o1}))^2} + \frac{4}{3}KTR_G = \frac{4KT\gamma}{(g_{m1})} + \frac{4}{3}KTR_G, \quad \text{(Eq 3.7)}$$

To further reduce IRN, as shown in Figure 3.9, a current reuse technique is utilized to double the effective transconductance for the same current, hence the IRN is decreased by half. For this structure, the input referred noise density is calculated,

$$\overline{V_{n,in}^2} = 4KT(\gamma g_{m1} + \gamma g_{m2}) \times (r_{o1}||r_{o2})^{\,2} \times \frac{1}{((g_{m1}+g_{m2})(r_{o1}||r_{o2}))^{\,2}} + \frac{4}{3}KTR_G$$

$$= \frac{4KT\gamma}{(g_{m1}+g_{m2})} + \frac{4}{3}KTR_G, \qquad \text{(Eq 3.8)}$$

Moreover, a differential input is needed to minimize the supply noise effect and also to connect 2-port µcoil to the LNA. So, for the first stage, a differential common-source current reuse structure is designed to have the least IRN possible in the desired bandwidth. For this stage, IRN, bandwidth, gain, area, and power consumptions are the required characteristics respectively in the order of importance.

But this stage is a differential-input to differential output, so another stage is needed to convert it to single output for connection to the single-ended spectrometer. Also, having several stages helps distributing the voltage gain across them, allowing to put the design focus for each stage on other parameters (e.g., noise for the first stage). So, another stage, which is an operational transconductance amplifier (OTA) in the form of a differential pair connected to an active load is designed to convert the differential-output to a single-ended output while increasing the gain. Since the input voltage has been magnified by the preamplifier and the first stage, the noise contribution of this stage is not important due to its negligible impact on the LNA's IRN. So, for designing this stage, bandwidth, gain, area, and power consumption are the important performance metrics, in the order of importance.

But these two stages cannot connect directly together and maintain the desired bandwidth. This is because the high input impedance of the mentioned common-source differential pair in the output stage causes a dominant pole at the output of the first stage, consequently killing the LNA's bandwidth. So, another stage was added in between to

increase the bandwidth. For this purpose, a differential common gate stage is added, which has a well-controlled low input resistance ($\frac{1}{gm_{N5,6}}$) that shoots the pole at the output of the first stage to a very high frequency. Similarly, to ensure that the input impedance of the differential pair at the output stage does not cause a dominant pole at the output of the 2nd stage, resistive loads (R1 and R2) are added to ensure a very small time constant at the output node of the second stage. For this stage bandwidth, gain, space, and power consumption are the critical characteristics respectively based on their importance. The final LNA structure is shown in the Figure 3-9. The total gain of this LNA is calculated,

$$A_v = (g_{m,N1} + g_{m,P1})\left(r_{o,N1}||r_{o,P1}\,||\frac{1}{g_{m,N5}}\right) \times \left(R1 \times g_{m,N5}\right) \times (g_{m,N3} \times (r_{o,N3}||r_{o,P4})),$$

(Eq 3.9)

In this design, one biasing resistor is needed at each input nodes, which connects the input transistors to the biasing voltage) to avoid short-circuiting of the LNA's input nodes. These resistors should be small since they affect the LNA input noise. N1, N2, P1 and P2 are designed in a way to have the least noise. For doing so, first the optimal current density (J) for the least noise is achieved for both NMOS and PMOS. This is done by doing noise analysis and plotting NF-min over V_{gs}. Since the gates of N1 and P1 (N2 and P2) are connected together, so their V_{gs} affecting each other, hence an optimal V_{gs} cannot be reached for both N1 and P1 and there is a trade-off. By some compromise, the optimal V_{gs} was achieved for the N-P connections. Based on the optimal J and the current which is chosen for a desired power consumption, size of N1, N2, P1, and P2 is set. For N0, the size is chosen so that it has less current variation due to V_{ds} changes, while generating the

required current for the first stage. N5 and N6 determines the bandwidth of the first stage by changing the output impedance from $ro_{N1}||ro_{P1}$ to $\frac{1}{gm_{N5,6}}$ while decreasing its gain by a factor of $\frac{1}{gm_{N5,6}}$. But since this stage has a gain of $gm_{N5,6} \times R1,2$, the total gain does not change. The sizing of N5, N6 is set based on their gm to obtain the desired bandwidth. For designing R1 and R2, first the third stage should be designed. The third stage bandwidth is proportional to $\frac{1}{ro_{N8}||ro_{P4}}$, while its gain is calculated by $gm_{N8} \times ro_{N8}||ro_{P4}$. So, based on the output swing and bandwidth (hence gm), $V_{gs,N7,8}$ is obtained which is set by the R1, and R2. So, while designing R1 and R2, in addition to the second stage gain and bandwidth, the biasing voltage of the third stage should be considered. The sizing of N7, N8, P2, and P3 is done based on the thirds stage gain and bandwidth. Design details are reported in the Table 3.5.

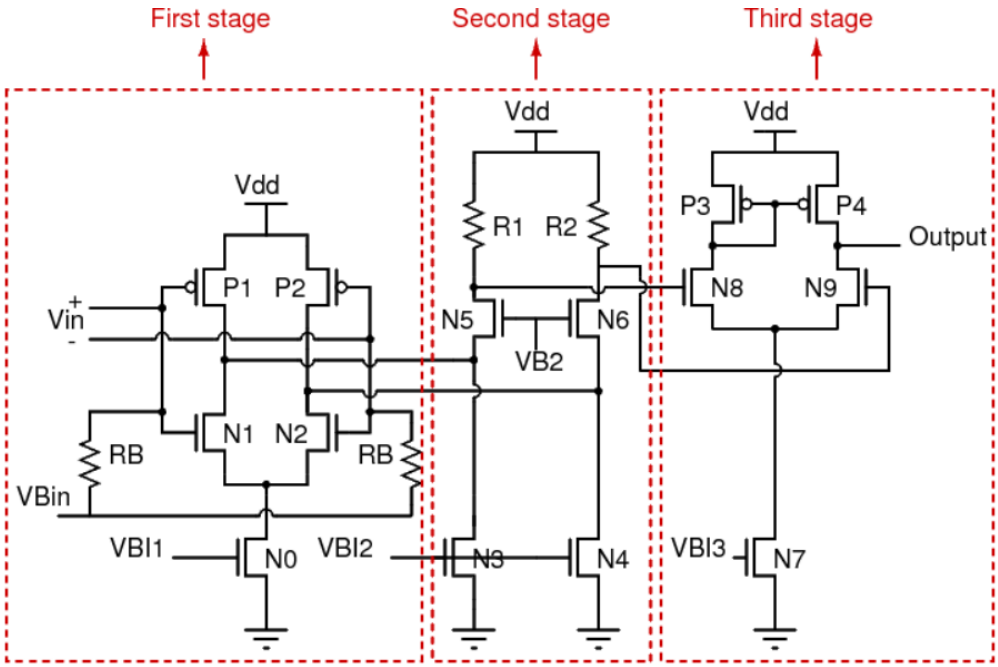

Figure 3-9 Circuit schematic of the designed 3-stage wideband LNA.

Table 3-5 LNA design details

$\frac{W}{L}_{N0} = \frac{288}{0.4}$, NG=20	RB= 50 Ω
$\frac{W}{L}_{N1,N2} = \frac{280}{0.35}$, NG=20	R1=R2= 500 Ω
$\frac{W}{L}_{N3,N4} = \frac{115.8}{0.35}$, NG=12	VBin= 1.1 V
$\frac{W}{L}_{N5,N6} = \frac{30}{0.35}$, NG=6	VBI1= 0.9 V
$\frac{W}{L}_{N7} = \frac{600}{0.35}$, NG=26	VB2= 1.6 V
$\frac{W}{L}_{N8,N9} = \frac{50}{0.35}$, NG=4	VBI2=0.8 V
$\frac{W}{L}_{P1,P2} = \frac{307}{0.35}$, NG=20	VBI3=0.8 V
$\frac{W}{L}_{P3,P4} = \frac{120}{0.35}$, NG=6	Vdd=2.1 V

3.2.3. Post Layout Simulation Result

The LNA's layout is shown in the Figure 3-10. It occupies an area of $130\ \mu m \times 137\ \mu m$.

For the post-layout to match with the simulation layout and have less parasitic effects, the symmetry of the circuit is maintained, while try to have the components close to each other for avoiding long wires and minimizing the layout area. Also, it was tried not to have different metal layers on top of each other to avoid parasitic capacitor creating by them. Moreover, the width of the wires was considered while designing the layout to have low parasitic capacitance while having small resistance which are in contrast with each other.

Based on the post layout simulations, the designed LNA has a bandwidth of about $600\ MHz$ (Figure 3-11), an input referred noise power spectral density (Figure 3-15) and a voltage gain (Figure 3-11) of $1.59\ \frac{nV}{\sqrt{Hz}}$ and $27\ dB$, respectively, both at $500\ MHz$, and a power consumption of $22.68\ mW$. These results meet the design requirements.

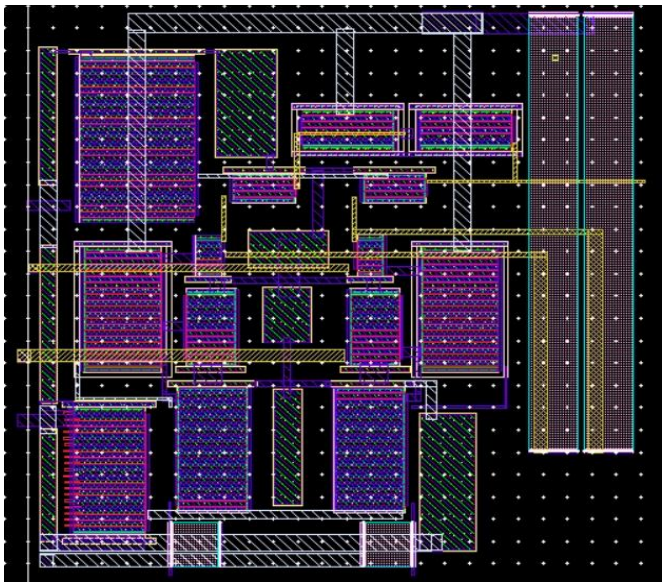

Figure 3-10 Layout of the designed 3-stage wideband LNA.

Due to the layout parasitic, even though in designing the layout it was tried to avoid these parasitic, the post-layout simulation differs with the pre-layout simulation. Based on the schematic design the designed LNA has a bandwidth of about $955\ MHz$ (Figure 3-12), an input referred noise power spectral density and a voltage gain (Figure 3-12) of $1.23\ \frac{nV}{\sqrt{Hz}}$ and $30.04\ dB$, respectively, both at $500\ MHz$, and a power consumption of $26.68\ mW$. Schematic and layout results are shown in Figure 3-12. As is shown in Figure 3-11 and 3-12, gain changes in our desired bandwidth (450 MHz to 550 MHz). Knowing these variations and knowing the gain at each frequency, the detected signals in the spectrometer could be adjusted. For example, if the gain at 500 MHz is 0.5 dB smaller than the gain at 450 MHz, at the spectrum, we consider this difference in the signal peaks at 500 and 450 MHz and reduce the peak amplitude at 450 MHz by 0.5 dB to have the same gain as the signal at 500 MHz.

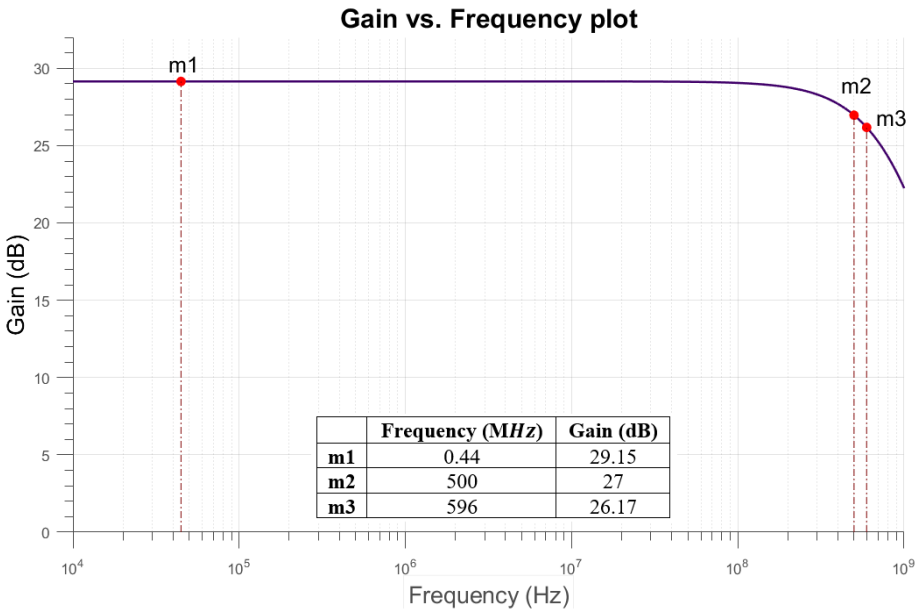

	Frequency (MHz)	Gain (dB)
m1	0.44	29.15
m2	500	27
m3	596	26.17

Figure 3-11 LNA gain and bandwidth post-layout results.

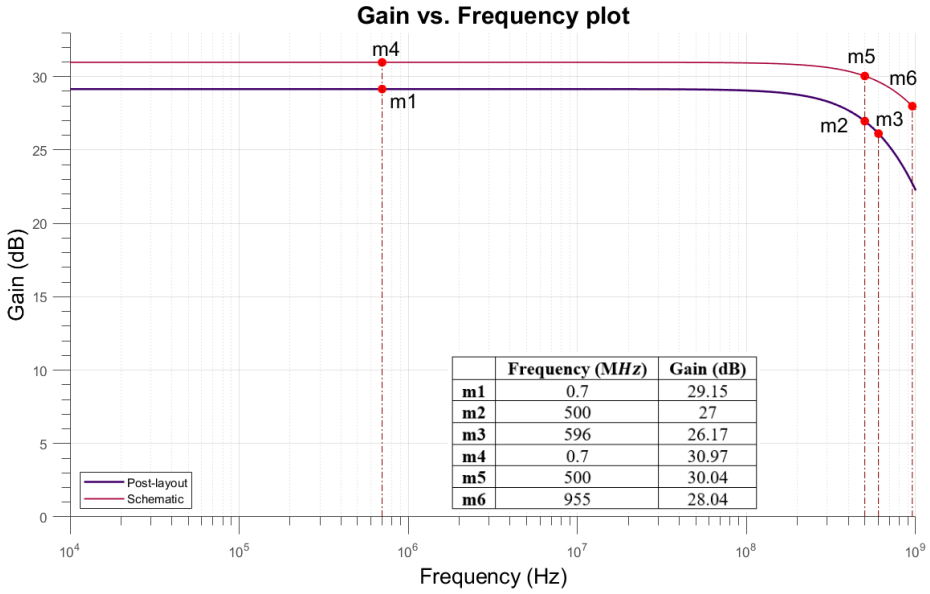

	Frequency (MHz)	Gain (dB)
m1	0.7	29.15
m2	500	27
m3	596	26.17
m4	0.7	30.97
m5	500	30.04
m6	955	28.04

Figure 3-12 Layout and schematic LNA gain and bandwidth comparison.

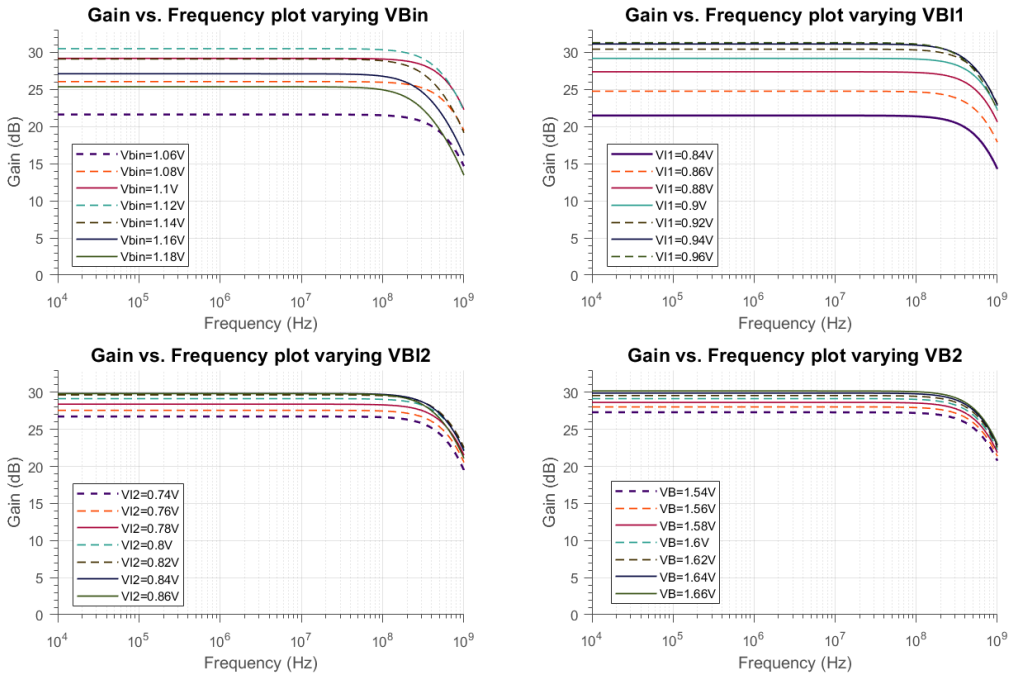

Figure 3-13 Gain and bandwidth changes due to biasing voltages variation (post-layout results).

Since the biasing voltages are coming from outside of the chip, their deviation from the nominal values should be considered while designing the PCB. The effect of biasing voltages variation on the gain and bandwidth is shown in Figure 3-13. Based on these results, the first stage biasing voltage variation affect the LNA properties considerably, on the other hand the second and third stage biasing have negligible effect on the results.

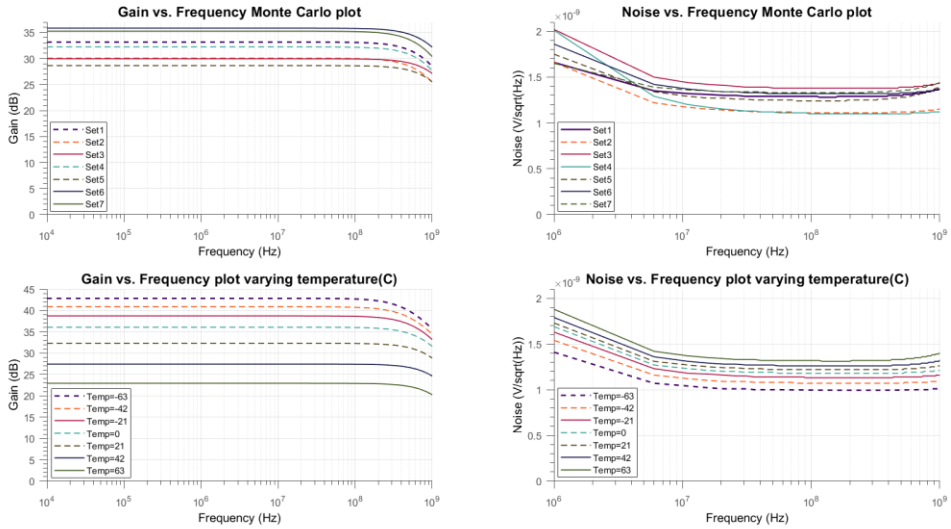

Figure 3-14 Monte Carlo simulation results.

In the figure above, the Monte Carlo simulation results are presented for both process variation and mismatch. Based on these results, our LNA works properly considering fabrication variations. Also, the temperature variation (-63º C to 63º C) effect on the results have been shown in this figure. Figures 3-13 and 3-14 demonstrate that our circuit performs properly considering biasing voltages variation, fabrication process variation, mismatch among components, and temperature changes.

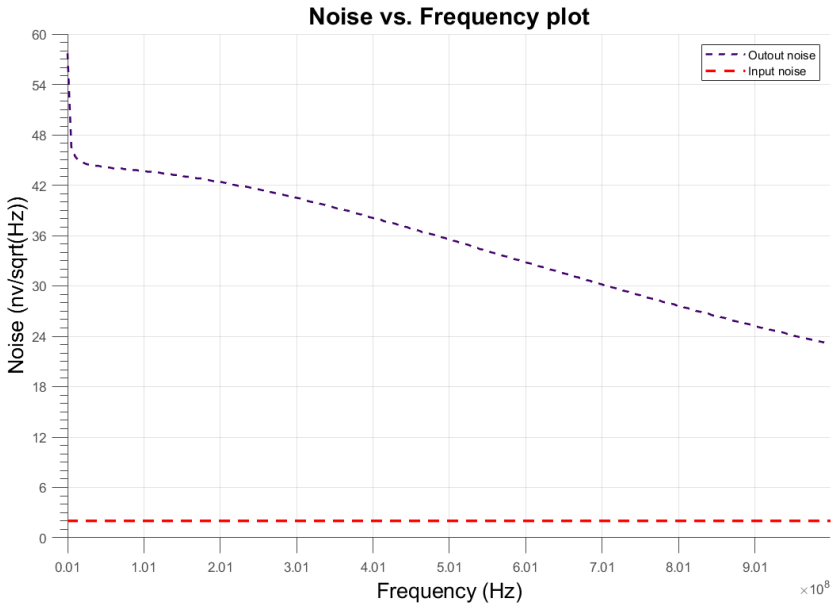

Figure 3-15 Input and output referred noise post-layout results.

Table 3.6 compares the presented LNA with the state-of-the-art in terms of gain, noise, bandwidth, and power consumption, illustrating the overall superior performance of the presented circuit compared to the state-of-the-art. It must be mentioned that the results from our work are from post-layout simulations, while most of the numbers from cited references are experimentally measured quantities.

Table 3-6 Comparison among CMOS NMR LNAs

References	*Gain(dB)*	*IRN* ($\frac{nV}{\sqrt{Hz}}$)	*Frequency (MHz)*	*Power (mW)*	*Technology (μm)*
[52]	30*	-	-	≤59.4	0.35
[48]**	14	3.4	85	-	0.8
[29]*	24	2.5	350	-	0.5
[56]*	42	0.78	300	-	0.13
[50]**	35	-	300	≤40	0.13
[33]**	-	1.3	300	≤18	0.13
Our work*	29.1	1.59	500	22.68	0.35

***: Post layout simulation**

****: Experimental**

3.3. Buffer

The data analysis units, such as the spectrometer and the signal processing unit, are placed outside of the NMR system, in a distance up to a few meters. So, the signal induced on the μcoil, which is amplified by the LNA, should travel all this distance before being processed. To minimize the loss of signal energy, a matching circuit is required to match the LNA's output impedance with the cable. Also, an active voltage buffer is typically used to make the output of the LNA a low-impedance node, resulting in minimizing the interference coupled onto the signal before reaching the spectrometer.

In some NMR systems, a mixer is used to down-convert the high frequency RF signal to baseband frequencies where the losses are significantly lower [31], [50], [53], [54].

3.3.1. Desired Characteristics

The purpose of the buffer is to convert the LNA output impedance to $50\,\Omega$, the cable impedance, while maintaining the bandwidth and gain. It should be noted that the output of the buffer is connected to the chip's I/O pad before being connected to the spectrometer cable. This means that it should be able to drive the pad's capacitance without losing the bandwidth. For this purpose, and based on the LNA's third stage, which is connected to the buffer, a simple PMOS buffer structure proposed in the Figure 3-16 is designed carefully. For an NMOS buffer, considering output DC voltage of the LNA which biases one of the NMOS transistors, to achieve the desired g_m generating the impedance in a limited current, having both NMOSs in the saturation mode was not possible. The sizing cannot increase due to the bandwidth limitation, hence for generating the current required for the g_m, only V_{gs} should be increased. With high V_{gs}, for having transistors in saturation modes, V_{ds} should be high, which due to the limitation in VDD we could not have both NMOS transistors in saturation region. For this reason, a PMOS structure is chosen over an NMOS one. The output impedance is calculated by *Eq* 3.10.

$$R_{out} = \frac{1}{g_{m,P0}+g_{mb,P0}} || R_{o,P1}. \qquad \text{(Eq 3.10)}$$

The DC voltage VI is adjustable, which allows for adjusting the buffer's bias current, hence $g_{m,P0}$ and consequently the output impedance of the circuit. This allows for fine-tuning the matching of the buffer's output impedance to the cable's impedance at the beginning and throughout the operation. Design details are reported in Table 3.7.

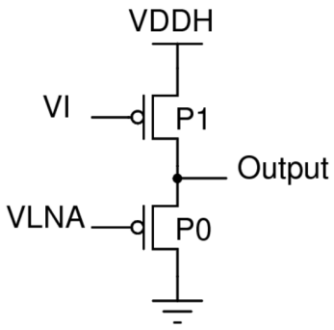

Figure 3-16 Buffer schematic.

Table 3-7 Buffer design details

$(\frac{\boldsymbol{W}}{\boldsymbol{L}})_{\boldsymbol{P0}} = \frac{\boldsymbol{150u}}{\boldsymbol{0.35u}}$	VI=1.7 V
$(\frac{\boldsymbol{W}}{\boldsymbol{L}})_{\boldsymbol{P1}} = \frac{\boldsymbol{190u}}{\boldsymbol{0.35u}}$	VDDH= 3.3V

The bandwidth should be higher than $500\ MHz$, and the gain which is calculated based on the *Eq* 3.11 should be maximized.

$$Gain = \frac{g_{m,P0} \times R_{out,P1}}{1 + g_{m,P0} \times R_{out,P1}} \quad \text{(Eq 3.11)}$$

3.3.2. Post Layout Simulation Results

Post layout simulations have been performed with and without the pad capacitor effect on the results is shown in Figure 3-17. The buffer have a voltage gain of -2.82 dB with a bandwidth up to a few $GHzs$, and power consumtion of 25 mW. The pad have no influence on the gain, on the other hand, it reduces the bandwidth. But even with the pad effect, the buffer bandwidth is more than 1 GHz.

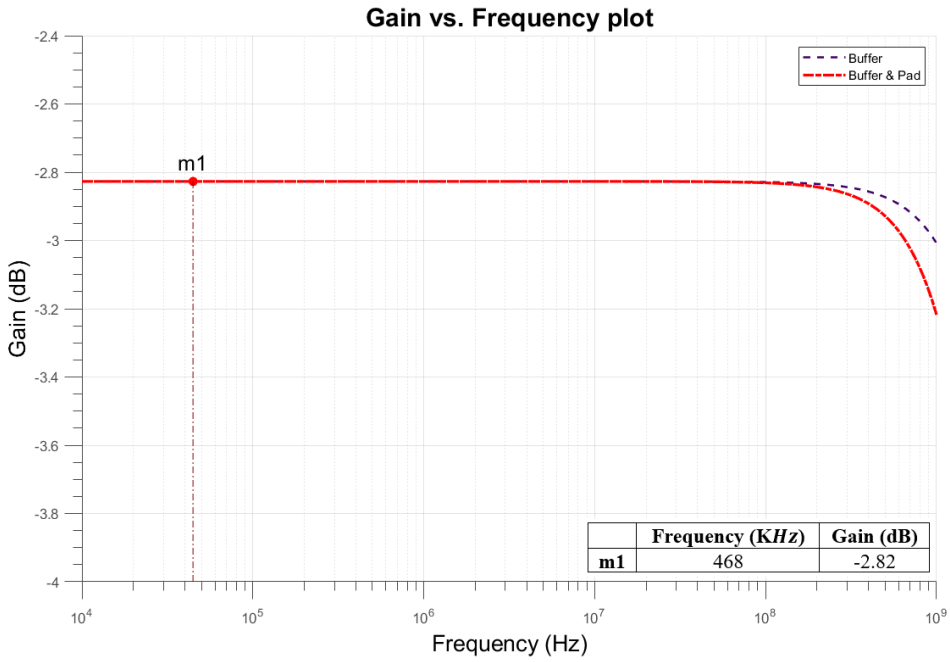

Figure 3-17 Gain and bandwidth for only buffer (black), and buffer with pad (red).

3.4. Readout System Integration

As mentioned previously, two channels are implemented on the chip. Channel 1 has an on-chip µcoil, a tuning variable capacitor, an LNA, and a buffer, while channel 2 has only a tuning variable capacitor, an LNA, and a buffer and is designed for an off-chip µcoil with characteristics provided by our collaborator. The chip schematic is shown in Figure 3-18. Also, the pins configuration is reported in Table 3.8.

Table 3-8 Pin configuration

1-***Gnd***	8- VIS2	15- OutOn
2-***Gnd***	9- VIS1	16-CLKon
3-***Gnd***	10- VBin	17- CapOn
4-***Vdd***=2.1 V	11- In+	18-CLKoff
5-***Vdd***=2.1 V	12- In-	19- CapOff
6-VBuff	13- OutOff	20- GND ESD
7-VgateS2	14- VDDH=3.3 V	21- VDD ESD

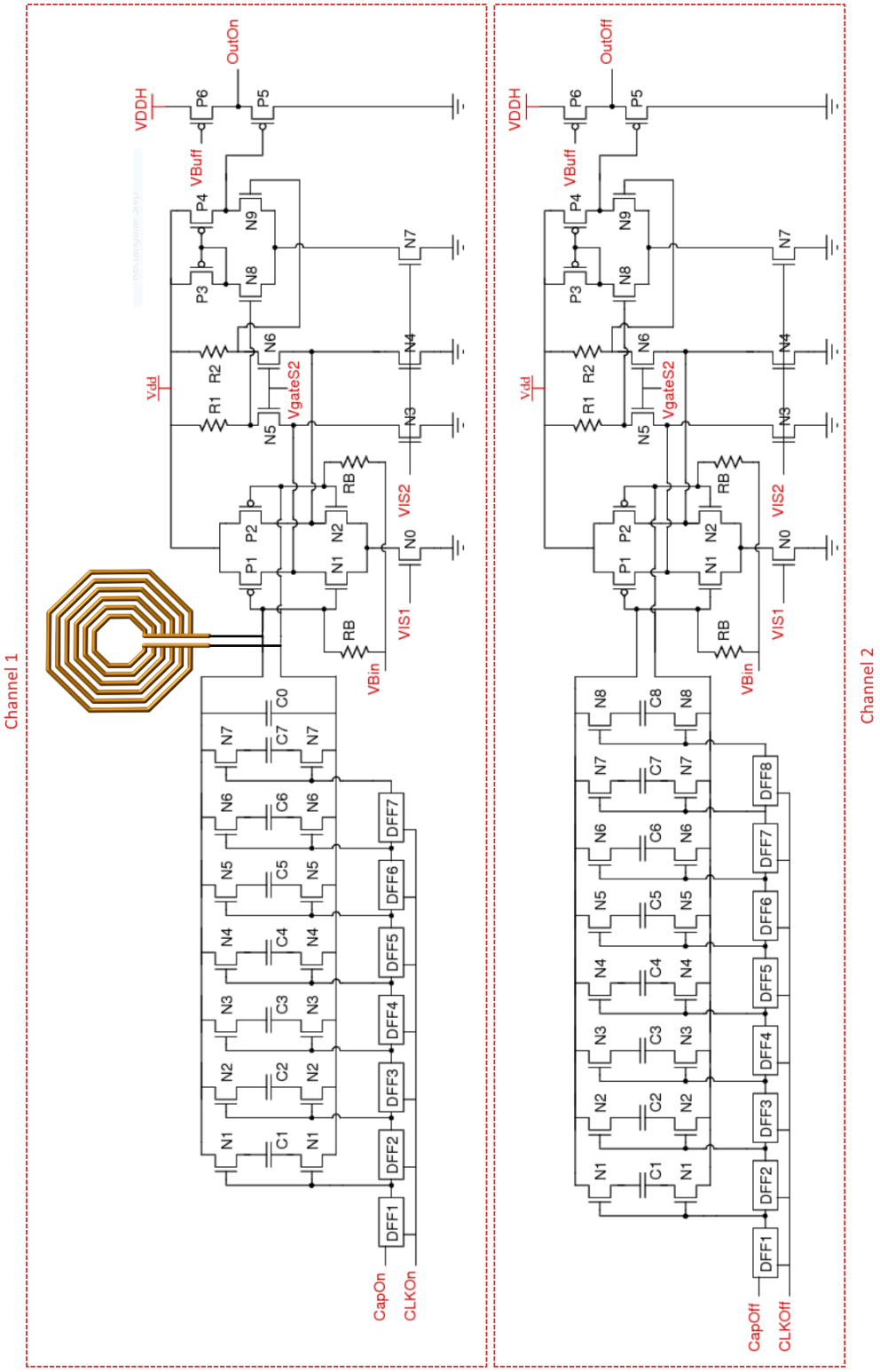

Figure 3-18 Chip schematic.

3.4.1. Post Layout Simulations

The complete layout of the presented chip is shown in Figure 3-19, which occupies an area of $1240\ \mu m \times 1555\ \mu m$. Also, the post layout simulation result of the LNA connected to the buffers and pads is shown in the Figure 3-20. Based on these simulations, the chip has a gain of $25.95\ dB$, bandwidth of $550\ MHz$, input referred noise power spectral density of 1.57 $\frac{nV}{\sqrt{Hz}}$, and a power consumption of 47.17 mW. Based on the earlier discussion, all of the obtained results from the post-layout simulation satisfy our design requirements.

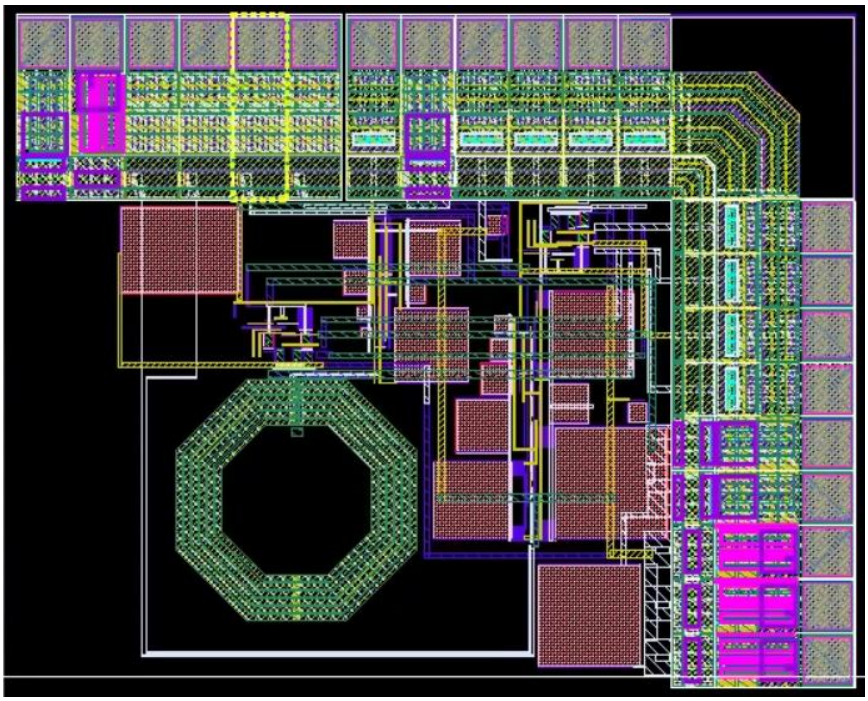

Figure 3-19 Chip layout.

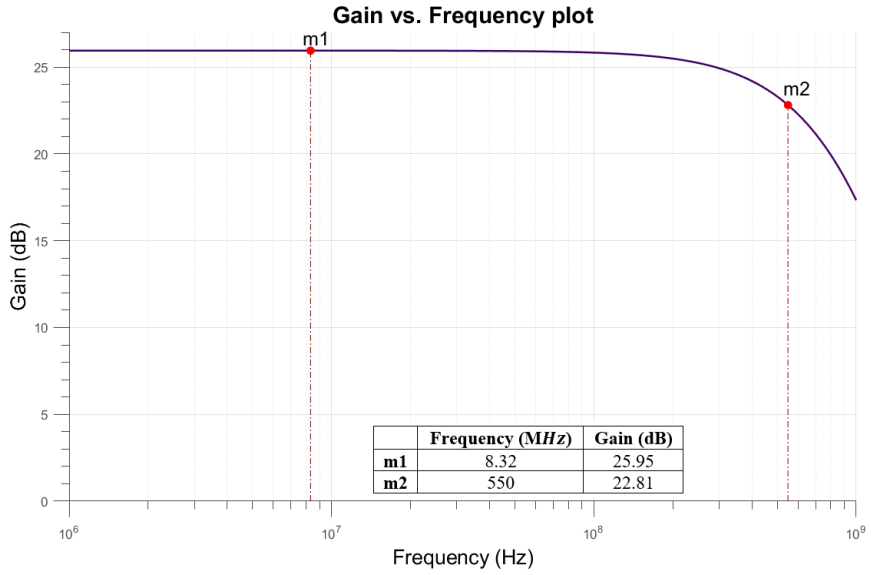

Figure 3-20 Chip gain and bandwidth post-layout results.

Chapter 4

Conclusions and Future Work

This chapter presents a summary of the proposed research, contributions, and possible future directions.

4.1. Conclusions

High-frequency NMR spectroscopy systems yield higher SNR, while facilitating a higher system throughput as they allow for integration of more parallel NMR receiving channels without the loss of performance. This motivated us for designing CMOS-based integrated active NMR receivers that operate at a higher frequency compared to the state-of-the-art. In this thesis an end-to-end design and optimization of an integrated NMR spectroscopy receiver (i.e., µcoil, tuning circuit, and readout front-end low-noise amplifier) operating at 500 MHz was presented. A two-channel fully-integrated NMR spectroscopy receiver was designed using AMS 0.35-µm technology compatible with a 500 MHz NMR spectroscopy device (Bruker). We identified all the important electrical and physical parameters in the design of a µcoil that could affect the NMR spectroscopy's overall performance. Consequently, we presented a design and optimization procedure for the

µcoil that takes all these parameters into account and is applicable to any frequency of operation. The integrated circuit is designed to be compatible with a wide range of on-chip and off-chip µcoils. Similar to the µcoil, the circuit architecture and the design procedure described for the readout circuit design is applicable to any frequency of operation This research contributes significantly to the development of a high-throughput high frequency NMR spectroscopy system, as described in the next section.

4.2. Contributions

The theoretical and design efforts presented in this thesis make the following contributions to the development of high-throughput NMR spectroscopy systems:

1. It is the first $500\ MHz$ NMR CMOS receiver compatible with a commercial NMR device (Bruker NMR system). While all components are designed and optimized for 500 MHz, the presented design procedures are applicable to higher frequencies.

2. The design of a CMOS-based µcoil is presented, which is optimized in terms of topology, number of layers, physical routing parameters, and geometrical shape, while considering the impact of CMOS process substrate and the sample's volume. Besides other factors already considered in the literature for designing NMR CMOS µcoils, this µcoil is optimized for the magnetic field uniformity as well.

3. A tuning circuitry is designed and integrated with the rest of the receiver components, in which instead of a fixed capacitor, a variable one is designed to compensate fabrication errors, sample effects, and make the chip compatible with different off-chip µcoils.

4. A low noise amplifier is designed and optimized with the smallest area and power consumption while meeting all the required performance metrics including input referred noise power spectral density, bandwidth, and voltage gain.

4.3. Future Work

As mentioned before, the successful outcome of this project opens a path towards the development of high-throughput high frequency NMR using multiple µcoils. This research was a starting step toward high-throughput NMR, but to achieve this goal several other steps need to be taken.

1- First of all this chip needs to be tested both electrically and experimentally. We have collaboration with University of Toronto A.SIMPSON group for the experimental part.

2- Based on the experimental results, the µcoil, and LNA could be improved if needed. For this purpose, instead of 0.35-μm a most recent technology node could be utilized that allows for a more area-efficient design, faster devices, and lower input referred noise for a lower power consumption. Also, more recent technology nodes offer more metal layers with thicker top metal layer, hence enabling us to have better µcoil design.

3- Number of channels should be increased. Also, here only the receiver part of the NMR system was designed. This chip could be enhanced by adding the transmitter part as well.

4- The sample delivery is another important part of the NMR device which was not a focus of this project. For improving the chip even more, an NMR-compatible microfluidic system could be added for sample delivery to the µcoil.

5- For a high-throughput device, the effect of channels on each other needs to be studied and minimized by simulating number of channels nearby. Mutual inductance of the different channels' µcoils is probably the most important factor to look for. One way to cancel the mutual inductance is by designing some external circuits, similar to [86]. Moreover, Isolating channels from each other is another way to reduce the crosstalk among them.

References

[1] R. Guha and E. Willighagen, “A Survey of Quantitative Descriptions of Molecular Structure,” *Curr. Top. Med. Chem.*, vol. 12, no. 18, pp. 1946–1956, Sep. 2012, doi: 10.2174/156802612804910278.

[2] M. Reichenbächer and J. Popp, *Challenges in Molecular Structure Determination*. Berlin, Heidelberg: Springer Berlin Heidelberg, 2012.

[3] H.-W. Wang and J.-W. Wang, “How cryo-electron microscopy and X-ray crystallography complement each other,” *Protein Sci.*, vol. 26, no. 1, pp. 32–39, Jan. 2017, doi: 10.1002/pro.3022.

[4] N. J. Rankin *et al.*, “The emergence of proton nuclear magnetic resonance metabolomics in the cardiovascular arena as viewed from a clinical perspective,” *Atherosclerosis*, vol. 237, no. 1, pp. 287–300, Nov. 2014, doi: 10.1016/j.atherosclerosis.2014.09.024.

[5] M. Carroni and H. R. Saibil, “Cryo electron microscopy to determine the structure of macromolecular complexes,” *Methods*, vol. 95, pp. 78–85, Feb. 2016, doi: 10.1016/j.ymeth.2015.11.023.

[6] A. T. Brünger, “X-ray crystallography and NMR reveal complementary views of structure and dynamics.,” *Nat. Struct. Biol.*, vol. 4 Suppl, pp. 862–5, Oct. 1997, [Online]. Available: http://www.ncbi.nlm.nih.gov/pubmed/9377160.

[7] J. C. A. Boeyens, “Molecular Structure,” in *New Theories for Chemistry*, Elsevier,

2005, pp. 177–227.

[8] B. Blümich and K. Singh, “Desktop NMR and Its Applications From Materials Science To Organic Chemistry,” *Angew. Chemie Int. Ed.*, vol. 57, no. 24, pp. 6996–7010, Jun. 2018, doi: 10.1002/anie.201707084.

[9] E. S. Mananga, “Efficient numerical integrator based on Fer expansion: Application to solid-state NMR experiments and to solve quantum Liouville equation and quantum Fokker-Planck equation,” *J. Adv. Phys.*, vol. 13, no. 4, pp. 4799–4803, 2017, doi: 10.24297/jap.v13i4.6011.

[10] P. C. A. van der Wel, “New applications of solid-state NMR in structural biology,” *Emerg. Top. Life Sci.*, vol. 2, no. 1, pp. 57–67, Apr. 2018, doi: 10.1042/ETLS20170088.

[11] A. K. Guha, “Application of NMR in Textiles , A Review,” no. December, 2020, doi: 10.5923/j.textile.20200902.01.

[12] A. Jancso *et al.*, “TDPAC and β-NMR applications in chemistry and biochemistry,” *J. Phys. G Nucl. Part. Phys.*, vol. 44, no. 6, 2017, doi: 10.1088/1361-6471/aa666b.

[13] J. Ginsberg, “NMR and MRI : Applications in Chemistry and Medicine NMR and MRI revolutionized the practice of chemistry and medicine by providing fast , non-destructive , and non-invasive means for the observation of matter from the atomic to the macroscopic scale .,” *Am. Chem. Soc. Natl. Hist. Chem. Landmarks. 2011*, 2011.

[14] A. L. Dunn and C. R. Landis, “Progress toward reaction monitoring at variable

temperatures: a new stopped-flow NMR probe design," *Magn. Reson. Chem.*, vol. 55, no. 4, pp. 329–336, 2017, doi: 10.1002/mrc.4538.

[15] P. A. BOTTOMLEY, "Spatial Localization in NMR Spectroscopy in Vivo," *Ann. N. Y. Acad. Sci.*, vol. 508, no. 1, pp. 333–348, 1987, doi: 10.1111/j.1749-6632.1987.tb32915.x.

[16] A. Abragam, *The Principles of Nuclear Magnetic Resonance*. 1961.

[17] K. C. Wong, "Review of NMR Spectroscopy: Basic Principles, Concepts and Applications in Chemistry NMR Spectroscopy: Basic Principles, Concepts and Applications in Chemistry; 3rd edition by HaraldGünther Wiley-VCH: Weinheim, Germany, 2013. xvi + 718 pp. ISBN 978-352733," *J. Chem. Educ.*, vol. 91, no. 8, pp. 1103–1104, Aug. 2014, doi: 10.1021/ed500324w.

[18] T. M. Nagy, K. E. Kövér, and O. W. Sørensen, "NORD: NO Relaxation Delay NMR spectroscopy," *Angew. Chemie Int. Ed.*, p. anie.202102487, Mar. 2021, doi: 10.1002/anie.202102487.

[19] J. Kim, B. Hammer, and R. Harjani, "A 5-300MHz CMOS transceiver for multi-nuclear NMR spectroscopy," *Proc. Cust. Integr. Circuits Conf.*, pp. 1–4, 2012, doi: 10.1109/CICC.2012.6330645.

[20] A. C. Dona *et al.*, "Precision High-Throughput Proton NMR Spectroscopy of Human Urine, Serum, and Plasma for Large-Scale Metabolic Phenotyping," *Anal. Chem.*, vol. 86, no. 19, pp. 9887–9894, Oct. 2014, doi: 10.1021/ac5025039.

[21] K. Lundquist, "Proton (1H) NMR Spectroscopy," 1992, pp. 242–249.

[22] G. L. Hoatson and R. L. Vold, “2H-NMR Spectroscopy of Solids and Liquid Crystals,” in *Solid-State NMR III Organic Matter*, Berlin, Heidelberg: Springer Berlin Heidelberg, 1994, pp. 1–67.

[23] I. Tkáć and R. Gruetter, “Methodology of1H NMR spectroscopy of the human brain at very high magnetic fields,” *Appl. Magn. Reson.*, vol. 29, no. 1, pp. 139–157, Mar. 2005, doi: 10.1007/BF03166960.

[24] V. V. Matveev *et al.*, “Investigation of Melts of Polybutylcarbosilane Dendrimers by 1H NMR Spectroscopy,” *Sci. Rep.*, vol. 7, no. 1, p. 13710, Dec. 2017, doi: 10.1038/s41598-017-13743-z.

[25] N. Sun, Y. Liu, H. Lee, R. Weissleder, and D. Ham, “CMOS RF Biosensor Utilizing Nuclear Magnetic Resonance,” *IEEE J. Solid-State Circuits*, vol. 44, no. 5, pp. 1629–1643, May 2009, doi: 10.1109/JSSC.2009.2017007.

[26] J. D. Trumbull, I. K. Glasgow, D. J. Beebe, and R. L. Magin, “Integrating microfabricated fluidic systems and NMR spectroscopy,” *IEEE Trans. Biomed. Eng.*, vol. 47, no. 1, pp. 3–7, 2000, doi: 10.1109/10.817611.

[27] D. . Hoult and R. . Richards, “The signal-to-noise ratio of the nuclear magnetic resonance experiment,” *J. Magn. Reson.*, vol. 24, no. 1, pp. 71–85, Oct. 1976, doi: 10.1016/0022-2364(76)90233-X.

[28] R. Pohmann, “Physical Basics of NMR,” 2011, pp. 3–21.

[29] G. Boero, J. Frounchi, B. Furrer, P. A. Besse, and R. S. Popovic, “Fully integrated probe for proton nuclear magnetic resonance magnetometry,” *Rev. Sci. Instrum.*,

vol. 72, no. 6, pp. 2764–2768, 2001, doi: 10.1063/1.1374599.

[30] S. G. Hyberts, S. A. Robson, and G. Wagner, “Exploring signal-to-noise ratio and sensitivity in non-uniformly sampled multi-dimensional NMR spectra,” *J. Biomol. NMR*, vol. 55, no. 2, pp. 167–178, 2013, doi: 10.1007/s10858-012-9698-2.

[31] J. Anders, J. Handwerker, M. Ortmanns, and G. Boero, “A fully-integrated detector for NMR microscopy in 0.13µm CMOS,” *Proc. 2013 IEEE Asian Solid-State Circuits Conf. A-SSCC 2013*, pp. 437–440, 2013, doi: 10.1109/ASSCC.2013.6691076.

[32] “NMR Instruments,” 2021. Bruker.com (accessed May 01, 2021).

[33] J. Anders, J. Handwerker, M. Ortmanns, and G. Boero, “A low-power high-sensitivity single-chip receiver for NMR microscopy,” *J. Magn. Reson.*, vol. 266, pp. 41–50, 2016, doi: 10.1016/j.jmr.2016.03.004.

[34] N. Zientek, C. Laurain, K. Meyer, M. Kraume, G. Guthausen, and M. Maiwald, “Simultaneous 19F-1H medium resolution NMR spectroscopy for online reaction monitoring,” *J. Magn. Reson.*, vol. 249, pp. 53–62, 2014, doi: 10.1016/j.jmr.2014.10.007.

[35] M. P. Ledbetter and D. Budker, “Zero-field nuclear magnetic resonance,” *Phys. Today*, vol. 66, no. 4, pp. 44–49, 2013, doi: 10.1063/PT.3.1948.

[36] A. J. Rossini, A. Zagdoun, M. Lelli, A. Lesage, C. Copéret, and L. Emsley, “Dynamic nuclear polarization surface enhanced NMR spectroscopy,” *Acc. Chem. Res.*, vol. 46, no. 9, pp. 1942–1951, 2013, doi: 10.1021/ar300322x.

[37] Q. Z. Ni *et al.*, “High frequency dynamic nuclear polarization,” *Acc. Chem. Res.*, vol. 46, no. 9, pp. 1933–1941, 2013, doi: 10.1021/ar300348n.

[38] H. J. Cho, J. Baugh, C. A. Ryan, D. G. Cory, and C. Ramanathan, “Low temperature probe for dynamic nuclear polarization and multiple-pulse solid-state NMR,” *J. Magn. Reson.*, vol. 187, no. 2, pp. 242–250, 2007, doi: 10.1016/j.jmr.2007.04.012.

[39] M. M.-F. Lam, “High-resolution nuclear magnetic resonance microspectroscopy,” University of Illinois at Urbana-Champaign, 1999.

[40] J. H. Grimes and T. M. O’Connell, “The application of micro-coil NMR probe technology to metabolomics of urine and serum,” *J. Biomol. NMR*, vol. 49, no. 3–4, pp. 297–305, 2011, doi: 10.1007/s10858-011-9488-2.

[41] R. M. Fratila, M. V. Gomez, S. Sýkora, and A. H. Velders, “Multinuclear nanoliter one-dimensional and two-dimensional NMR spectroscopy with a single non-resonant microcoil,” *Nat. Commun.*, vol. 5, no. 1, p. 3025, May 2014, doi: 10.1038/ncomms4025.

[42] I. Fugariu *et al.*, “Towards single egg toxicity screening using microcoil NMR,” *Analyst*, vol. 142, no. 24, pp. 4812–4824, 2017, doi: 10.1039/C7AN01339F.

[43] J. Deborne, N. Pinaud, and Y. Crémillieux, “Implantable NMR Microcoils in Rats: A New Tool for Exploring Tumor Metabolism at Sub-Microliter Scale?,” *Metabolites*, vol. 11, no. 3, p. 176, Mar. 2021, doi: 10.3390/metabo11030176.

[44] Y. Crémillieux *et al.*, “Online Quantification of Lactate Concentration in Microdialysate During Cerebral Activation Using 1H-MRS and Sensitive NMR

Microcoil," *Front. Cell. Neurosci.*, vol. 13, Mar. 2019, doi: 10.3389/fncel.2019.00089.

[45] D. L. Olson, T. L. Peck, A. G. Webb, R. L. Magin, and J. V. Sweedler, "High-Resolution Microcoil 1H-NMR for Mass-Limited, Nanoliter-Volume Samples," *Science (80-.).*, vol. 270, no. 5244, pp. 1967–1970, Dec. 1995, doi: 10.1126/science.270.5244.1967.

[46] K. Hashi *et al.*, "Achievement of 1020 MHz NMR," *J. Magn. Reson.*, vol. 256, pp. 30–33, 2015, doi: 10.1016/j.jmr.2015.04.009.

[47] N. Sun, T. J. Yoon, H. Lee, W. Andress, R. Weissleder, and D. Ham, "Palm NMR and 1-chip NMR," *IEEE J. Solid-State Circuits*, vol. 46, no. 1, pp. 342–352, 2011, doi: 10.1109/JSSC.2010.2074630.

[48] T. Cherifi *et al.*, "A CMOS microcoil-associated preamplifier for NMR spectroscopy," *IEEE Trans. Circuits Syst. I Regul. Pap.*, vol. 52, no. 12, pp. 2576–2583, 2005, doi: 10.1109/TCSI.2005.857870.

[49] T. H. Rehm *et al.*, "Continuous-flow synthesis of fluorine-containing fine chemicals with integrated benchtop NMR analysis," *React. Chem. Eng.*, vol. 2, no. 3, pp. 315–323, 2017, doi: 10.1039/C7RE00023E.

[50] M. Grisi, G. M. Conley, P. Sommer, J. Tinembart, and G. Boero, "A single-chip integrated transceiver for high field NMR magnetometry," *Rev. Sci. Instrum.*, vol. 90, no. 1, 2019, doi: 10.1063/1.5066436.

[51] H. Davoodi, M. Jouda, J. G. Korvink, N. MacKinnon, and V. Badilita, "Broadband

and multi-resonant sensors for NMR," *Prog. Nucl. Magn. Reson. Spectrosc.*, vol. 112–113, pp. 34–54, 2019, doi: 10.1016/j.pnmrs.2019.05.001.

[52] J. Anders, P. SanGiorgio, and G. Boero, "An integrated CMOS receiver chip for NMR-applications," *Proc. Cust. Integr. Circuits Conf.*, no. Cicc, pp. 471–474, 2009, doi: 10.1109/CICC.2009.5280786.

[53] J. Anders, P. Sangiorgio, and G. Boero, "A fully integrated IQ-receiver for NMR microscopy," *J. Magn. Reson.*, vol. 209, no. 1, pp. 1–7, 2011, doi: 10.1016/j.jmr.2010.12.005.

[54] M. Grisi, G. Gualco, and G. Boero, "A broadband single-chip transceiver for multi-nuclear NMR probes," *Rev. Sci. Instrum.*, vol. 86, no. 4, 2015, doi: 10.1063/1.4916206.

[55] J. Anders, G. Chiaramonte, P. SanGiorgio, and G. Boero, "A single-chip array of NMR receivers," *J. Magn. Reson.*, vol. 201, no. 2, pp. 239–249, 2009, doi: 10.1016/j.jmr.2009.09.019.

[56] H. Pourmodheji, E. Ghafar-Zadeh, and S. Magierowski, "A multidisciplinary approach to high throughput nuclear magnetic resonance spectroscopy," *Sensors (Switzerland)*, vol. 16, no. 6, 2016, doi: 10.3390/s16060850.

[57] S. Ha *et al.*, "Silicon-Integrated High-Density Electrocortical Interfaces," *Proc. IEEE*, vol. 105, no. 1, pp. 11–33, 2017, doi: 10.1109/JPROC.2016.2587690.

[58] A. Rikhter and M. M. Fogler, "Inductor coil of the highest possible Q," *Sci. Rep.*, vol. 10, no. 1, pp. 1–9, 2020, doi: 10.1038/s41598-020-72308-9.

[59] D. L. Olson, M. E. Lacey, and J. V. Sweedler, “High-Resolution Microcoil NMR for Analysis of Mass-Limited, Nanoliter Samples,” *Anal. Chem.*, vol. 70, no. 3, pp. 645–650, Feb. 1998, doi: 10.1021/ac970972y.

[60] L. Renaud *et al.*, “Implantable planar rf microcoils for NMR microspectroscopy,” *Sensors Actuators, A Phys.*, vol. 99, no. 3, pp. 244–248, 2002, doi: 10.1016/S0924-4247(01)00914-1.

[61] Z. Ali, D. P. Poenar, and S. Aditya, “Design of planar microcoil-based NMR probe ensuring high SNR,” *AIP Adv.*, vol. 7, no. 9, 2017, doi: 10.1063/1.5002721.

[62] S. Jannin, A. Bornet, S. Colombo, and G. Bodenhausen, “Low-temperature cross polarization in view of enhancing dissolution Dynamic Nuclear Polarization in NMR,” *Chem. Phys. Lett.*, vol. 517, no. 4–6, pp. 234–236, 2011, doi: 10.1016/j.cplett.2011.10.042.

[63] “1995,s-1.pdf.” .

[64] K. Ehrmann *et al.*, “Microfabricated solenoids and Helmholtz coils for NMR spectroscopy of mammalian cells,” *Lab Chip*, vol. 7, no. 3, pp. 373–380, 2007, doi: 10.1039/b614044k.

[65] C. Massin *et al.*, “Planar microcoil-based microfluidic NMR probes,” *J. Magn. Reson.*, vol. 164, no. 2, pp. 242–255, 2003, doi: 10.1016/S1090-7807(03)00151-4.

[66] H. Wensink *et al.*, “Measuring reaction kinetics in a lab-on-a-chip by microcoil NMR,” *Lab Chip*, vol. 5, no. 3, pp. 280–284, 2005, doi: 10.1039/b414832k.

[67] A. Substrates, “NMR Microspectroscopy Using 100,” vol. 41, no. 7, pp. 1992–1995,

1994.

[68] J. E. Stocker, A. G. Webb, T. L. Peck, M. Feng, and R. L. Magin, “Nanoliter volume, high-resolution NMR microspectroscopy using a 60-/m planar microcoil,” *IEEE Trans. Biomed. Eng.*, vol. 44, no. 11, pp. 1122–1127, 1997, doi: 10.1109/10.641340.

[69] C. Massin, G. Boero, F. Vincent, J. Abenhaim, P. A. Besse, and R. S. Popovic, “High-Q factor RF planar microcoils for micro-scale NMR spectroscopy,” *Sensors Actuators, A Phys.*, vol. 97–98, no. November 2001, pp. 280–288, 2002, doi: 10.1016/S0924-4247(01)00847-0.

[70] R. L. Ehman *et al.*, “Magnetic resonance,” *Radiology*, vol. 194, no. 3, pp. 933–940, 1995, doi: 10.1093/acprof:oso/9780198742906.003.0028.

[71] R. M. Fratila, M. V. Gomez, S. Sýkora, and A. H. Velders, “Multinuclear nanoliter one-dimensional and two-dimensional NMR spectroscopy with a single non-resonant microcoil,” *Nat. Commun.*, vol. 5, 2014, doi: 10.1038/ncomms4025.

[72] Y. Maguire, I. L. Chuang, S. Zhang, and N. Gershenfeld, “Ultra-small-sample molecular structure detection using microslot waveguide nuclear spin resonance,” *Proc. Natl. Acad. Sci. U. S. A.*, vol. 104, no. 22, pp. 9198–9203, 2007, doi: 10.1073/pnas.0703001104.

[73] R. Beiranvand, “Analyzing the uniformity of the generated magnetic field by a practical one-dimensional Helmholtz coils system,” *Rev. Sci. Instrum.*, vol. 84, no. 7, 2013, doi: 10.1063/1.4813275.

[74] H. G. Krojanski, J. Lambert, Y. Gerikalan, D. Suter, and R. Hergenröder, “Microslot

NMR probe for metabolomics studies," *Anal. Chem.*, vol. 80, no. 22, pp. 8668–8672, 2008, doi: 10.1021/ac801636a.

[75] P. J. M. van Bentum, J. W. G. Janssen, A. P. M. Kentgens, J. Bart, and J. G. E. Gardeniers, "Stripline probes for nuclear magnetic resonance," *J. Magn. Reson.*, vol. 189, no. 1, pp. 104–113, 2007, doi: 10.1016/j.jmr.2007.08.019.

[76] R. C. Meier, J. Höfflin, V. Badilita, U. Wallrabe, and J. G. Korvink, "Microfluidic integration of wirebonded microcoils for on-chip applications in nuclear magnetic resonance," *J. Micromechanics Microengineering*, vol. 24, no. 4, p. 045021, Apr. 2014, doi: 10.1088/0960-1317/24/4/045021.

[77] N. Ben Mansour, C. Dridi, N. Yaakoubi, and L. Fakri-Bouchet, "NMR Implantable Microcoil FEM Based Comparative Study for Numerical Brain Model Application," in *2019 IEEE International Conference on Design & Test of Integrated Micro & Nano-Systems (DTS)*, Apr. 2019, pp. 1–6, doi: 10.1109/DTSS.2019.8914833.

[78] Z. Ali, D. P. Poenar, and S. Aditya, "Design of planar microcoil-based NMR probe ensuring high SNR," *AIP Adv.*, vol. 7, no. 9, p. 095107, Sep. 2017, doi: 10.1063/1.5002721.

[79] G. Boero, C. De Raad Iseli, P. A. Besse, and R. S. Popovic, "An NMR magnetometer with planar microcoils and integrated electronics for signal detection and amplification," *Sensors Actuators, A Phys.*, vol. 67, no. 1–3, pp. 18–23, 1998, doi: 10.1016/S0924-4247(97)01722-6.

[80] C. R. Neagu, H. V. Jansen, A. Smith, J. G. E. Gardeniers, and M. C. Elwenspoek,

"Characterization of a planar microcoil for implantable microsystems," *Sensors Actuators, A Phys.*, vol. 62, no. 1–3, pp. 599–611, 1997, doi: 10.1016/S0924-4247(97)01601-4.

[81] L. Lin, W. Y. Yin, J. F. Mao, and Y. Y. Wang, "Implementation of new CMOS differential stacked spiral inductor for VCO design," *IEEE Microw. Wirel. Components Lett.*, vol. 17, no. 10, pp. 727–729, 2007, doi: 10.1109/LMWC.2007.905635.

[82] "ANSYS Workbench." ANSYS Inc, Canonsburg, PA, 2009.

[83] G. Giovannetti, "Comparison between circular and square loops for low-frequency magnetic resonance applications: theoretical performance estimation," *Concepts Magn. Reson. Part B Magn. Reson. Eng.*, vol. 46B, no. 3, pp. 146–155, Jul. 2016, doi: 10.1002/cmr.b.21343.

[84] I. Bertini, C. Luchinat, and G. Parigi, "Magnetic susceptibility in paramagnetic NMR," *Prog. Nucl. Magn. Reson. Spectrosc.*, vol. 40, no. 3, pp. 249–273, 2002, doi: 10.1016/S0079-6565(02)00002-X.

[85] H. Davoodi, N. Nordin, L. Bordonali, J. G. Korvink, N. MacKinnon, and V. Badilita, "An NMR-compatible microfluidic platform enabling: In situ electrochemistry," *Lab Chip*, vol. 20, no. 17, pp. 3202–3212, 2020, doi: 10.1039/d0lc00364f.

[86] S. M. Wright and L. L. Wald, "Theory and application of array coils in MR spectroscopy," *NMR Biomed.*, vol. 10, no. 8, pp. 394–410, Dec. 1997, doi: 10.1002/(SICI)1099-1492(199712)10:8<394::AID-NBM494>3.0.CO;2-0.

Appendix

The development of the associated printed board circuit (PCB) is tricky and several considerations should be taken into account. As mentioned above the NMR receiver which includes the integrated chip and its associated PCB, should be placed into a limited space. So, sizing of the PCB is really important and the PCB should be minimized. For this purpose, the discrete components should be chosen based on their size as well as other desired characteristics. Moreover, the placement of the components and the routing should be optimized.

Another crucial factor for selecting the PCB components, it's the NMR compatibility of them. Since this PCB is supposed to work in a huge static magnetic field, the components should be selected in a way that this magnetic field has no effect on their function. This property is called as NMR compatibility and is the most important features to consider while designing the PCB.

Additionally, designing the PCB output faces us with more challenges. The PCB output should be connected to the spectrometer through a coaxial cable which is connected to both ends via BNC connectors. But since the PCB is miniaturized, the chosen BNC connectors should be as small as possible, while being NMR compatible. This issue is applied to all the supply voltages as well. Also, the number of supply voltages that are coming externally should be minimized.

A block diagram of the estimated PCB is shown in figure below.

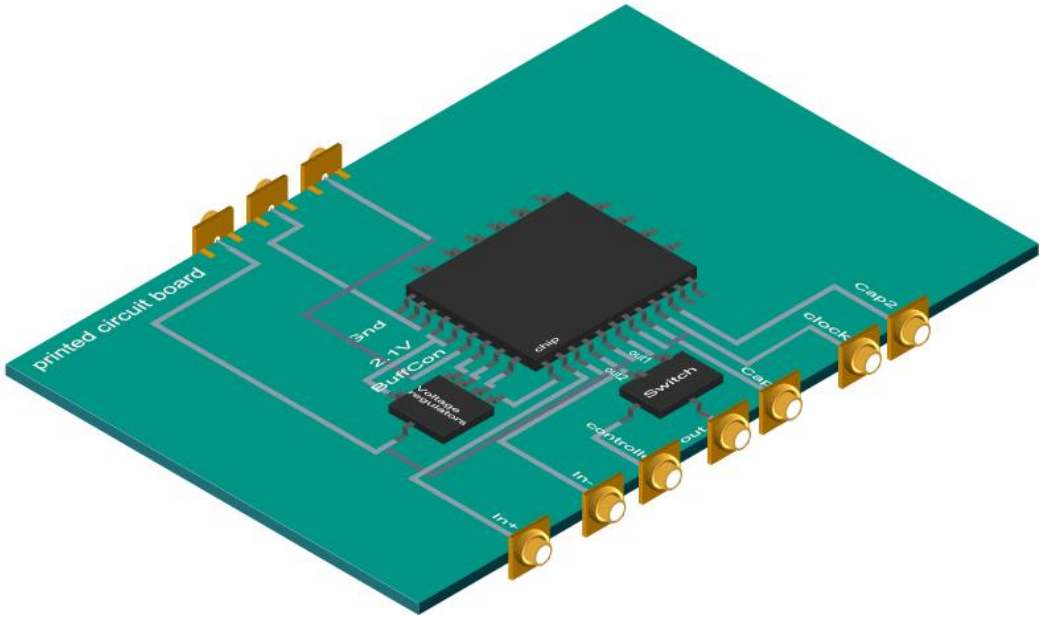

PCB overview

The detailed chip pin configuration from the bottom left side of the layout is described in the table below. Pin number of 1 to 15 are analog, while 16 to 21 are digital.

1-Gnd (all)	8- VIS2 (LNA second stage current source)	15- OutOn (Channel 1 output)
2-Gnd (all)	9- VIS1 (LNA first stage current source	16-CLKon (Channel 21capacitive circuitry clock)
3-Gnd (all)	10- VBin (LNA first stage input bias)	17- CapOn (Channel 1 capacitive circuitry input for the shift register)
4-Vdd=2.1 V (all except buffer)	11- In+ (Channel 2, positive node of coil/ positive input of the LNA)	18-CLKoff (Channel 2 capacitive circuitry clock)
5-Vdd=2.1 V (all except buffer)	12- In- (Channel 2, negative node of coil/ negative input of the LNA)	19- CapOff (Channel 2 capacitive circuitry input for the shift register)
6-VBuff (Buffer input controller)	13- OutOff (Channel 2 output)	20- GND ESD
7-VgateS2 (LNA second stage gate input)	14- VDDH=3.3 V (Buffers VDD)	21- VDD ESD

It should be noted that 2 different $vdds$ are used in this design. A 2.1V is used for all the circuit except buffer. For buffer a 3.3V vdd (VDDH) is used. Also, 3 pins are dedicated to gnd for ensuring that the circuit could use the required current.